

Two-phase flow void fraction estimation based on bubble image segmentation using Randomized Hough Transform with Neural Network (RHTN)



Pedro L.S. Serra^a, Paulo H.F. Masotti^b, Marcelo S. Rocha^b, Delvonei A. de Andrade^b, Walmir M. Torres^b, Roberto N. de Mesquita^{b,*}

^a Universidade Paulista – Instituto de Ciências Exatas e Tecnologia, Rua Dr. Bacelar, 1212 – Vila Clementino, 04026-002, São Paulo, SP, Brazil

^b Instituto de Pesquisas Energéticas e Nucleares (IPEN/CNEN - SP) – Centro de Engenharia Nuclear, Av. Lineu Prestes, 2242 - Cidade Universitária, 05508-000, São Paulo, SP, Brazil

ARTICLE INFO

Keywords:

Nuclear power plant
Fuzzy logic
Passive systems
Natural circulation
Two-phase flow
Artificial neural networks
Pattern recognition
Randomized Hough Transform
Void fraction

ABSTRACT

The International Atomic Energy Agency (IAEA) has been encouraging the use of passive cooling systems in new designs of nuclear power plants. Next nuclear reactor generations are intended to have simpler and robust safety resources. Natural Circulation based systems hold an undoubtedly prominent position among these. The study of limiting conditions of these systems has led to instability behavior analysis where many different two-phase flow patterns are present. Void fraction is a key parameter in thermal transfer analysis of these flow instability conditions. This work presents a new method to estimate void fraction from images captured of an experimental two-phase flow circuit. The method integrates a set of Artificial Neural Networks with a modified Randomized Hough Transform to make multiple scans over acquired images, using crescent-sized masks. This method was called Randomized Hough Transform with Neural Network (RHTN). Each different mask size is chosen according with bubble sizes, which are the main ‘objects of interest’ in this image analysis. Images are segmented using fuzzy inference with different parameters adjusted based on acquisition focus. Void fraction calculation considers the volume of the imaged geometrical section of flow inside cylindrical glass tubes considering the acquisition depth-of-field used. The bubble volume is estimated based on geometrical parameters inferred for each detected bubble. The image database is obtained from experiments performed on a vertical two-phase flow circuit made of cylindrical glass where flow-patterns visualization is possible. The results have shown that the estimation method had good agreement with increasing void fraction experimental values. RHTN has been very efficient as bubble detector with very low ‘false-positive’ cases (< 0.004%) due robustness obtained through integration between Artificial Neural Networks with Randomized Hough Transforms.

1. Introduction

One of the main objectives of research in new nuclear power plant projects is the simplification in order to reduce costs without affecting their safety and reliability. The purpose to develop safety passive systems applied to Water Cooled Reactors (WCR) is in plenty agreement with this goal (Cleveland and Choi, 2009).

Passive cooling systems could remove the residual heat of the core without using external power. These systems could improve the safety of nuclear power plants (Wang et al., 2012a). These systems have been enforced by IAEA as a desired method to simplify and increase essential safety functions in the next nuclear power plant generations (Cleveland

and Choi, 2009). Fukushima accident revealed the need for a detailed review in safety principles of newer nuclear power plants. The Co-ordinated Research Project (CRP) created by IAEA in 2004, presents studies where passive safety systems using natural circulation are described as economic and as having safety improvements when applied to nuclear plants. Costs reduction due to multiples pumps maintenance and corresponding operation are recommended for the passive systems. Passive safety system main purpose is to be applied during active cooling system failures, usually named Loss of Coolant Accident or LOCA, which may cause a nuclear power plant shutdown.

Cleveland and Choi (2009) have described an integrated research plan to: a) identify and describe reference systems; b) identify and

* Corresponding author. Centro de Engenharia Nuclear, room 32 Instituto de Pesquisas Energéticas e Nucleares, Av. Prof. Lineu Prestes, 2.242 - Cidade Universitária, 05508-000, São Paulo, SP, Brazil.

E-mail address: rnavarro@ipen.br (R.N. de Mesquita).

Nomenclature	
$A(c,r)$	ellipse tangent line point coordinates
a	Artificial neural network hidden layer element
a	major ellipse semi-axis (pixels)
A, B, C	General ellipse equation parameters
ANN	Artificial Neural Network
b	ANN bias
b	minor ellipse semi-axis (pixels)
b	linear coefficient
C	centroid location of output membership function
$C(c,r)$	ellipse center (column, row) coordinates (pixels)
FFIS	Focal Fuzzy Inference System
g	gravity acceleration (m/s^2)
I	normalized gray intensity
$I^{(-)}$	complementary (negative) normalized gray intensity
IL	complementary (negative) normalized gray intensity added with Laplacian
IS	normalized complementary gray intensity added with Sobel
$J(.)$	ANN cost function
L	Laplacian operator – second directional derivative
L	pressure tap's high difference
m	angular coefficient
P	u-tube manometer water level pressure
RHT	Randomized Hough Transform
RHTN	Artificial Neural Network integrated with Randomized Hough Transform
S	Sobel operator – first directional derivative
S	sample upper area (mm^3)
S	sample front view (mm)
u	ANN linear combinator
v	ANN linear induced field
X	ANN input signal element
x	vectorized ANN input
(x,y)	ellipse (column, row) coordinates (pixels)
y	ANN neuron output
w	synaptic weight element
W	synaptic weight matrix
<i>Greek Symbols</i>	
α	void fraction (estimation)
$<\alpha>$	average void fraction (experimental)
δ	uncertainty
δ	experimental void fraction
$\Delta\Delta$	difference
γ	void fraction estimation ratio
ε	void fraction (estimation)
$\varphi(.)$	activation function
Φ	diameter (pixels)
λ	adjustment factor
$\mu(.)$	membership function
μ	average
ρ	density (kg/m^3)
σ	standard deviation
θ	ellipse major-axis inclination
<i>Subscripts</i>	
b	border pixel
c	center
dof	depth-of-field
gl	gas-liquid
exp	experimental data
ext	external
G	gas
if	in-focus
int	internal
L	liquid
o	reference system origin
0	initial value
oof	out-of-focus
og	centroid
$RHTN$	RHTN estimation
sc	shape center
xy	image directions
k	neuron index
m	last input signal element
m	medium point coordinates
t	tangent point coordinates
<i>Superscripts</i>	
$-$	(upper bar) average value
$(-)$	complementary or negative value
T	transpose

characterize phenomena that influence natural circulation; c) make reliable analyses and d) do evaluations of passive safety systems with designs that use natural circulation as basis. Most of these studies intend to obtain a representative model to evaluate parameters related to natural circulation phenomena.

Studies have shown that a small portion of heat decay was transferred to moderator by radiation in the Advanced Heavy Water Reactor (AHWR) design. This feature would lead to long periods of plant blackout operations, increasing the moderator temperature and pressure. Alternative design suggests that incorporating natural circulation should keep the moderator within safety limits for at least seven days (Kumar et al., 2015).

Some reactors of new generation make use of natural circulation systems for heat removal in case of shutdown. It has been applied in pressurized water-cooled power reactors (PWR) and pressurized heavy water reactors (PHWR). These new systems proved to be effective in removing up to 20% of the reactor nominal power (Kudariyawar et al., 2016).

Natural circulation cooling systems have been used in other

engineering applications such as solar heating systems, cooling mechanisms of internal combustion engines, geothermal power extraction and computer systems.

A safety study of natural circulation cooling systems was done at Kyoto University Research Reactor (Zhang et al., 2015). Experiments were performed in the 10–100 kW power range where shutdown was included as one of the conditions. Temperature measurements were performed at many different circuit positions. Flow velocities along the reactor core pointed out that safety criteria were satisfied at most critical condition (100 kW operating power).

Many works as Sunde et al. (2005), Wang and Dong (2009), Fichera et al. (2000), Crivelaro et al. (2002) and De Mesquita et al. (2012) have been made to automatically (using artificial intelligence techniques) find relations between experimentally acquired images from natural circulation circuits and their correspondent two-phase flow patterns.

Barbosa et al. (2010) uses Self-Organizing Map (SOM) to classify two-phase flow patterns in an experiment with horizontal forced circulation. Experimental measurements of capacitance, pressure drop, and pressure gradients were used as training and testing parameters to

SOMs. Classification results were based on six different flow patterns. A transient phase between bubble and churn flow was mentioned as an essential parameter and identifier of the flow behavior along the circuit and void fraction was considered a key estimated parameter (Barbosa et al., 2010) and (Smith et al., 2012).

Such studies were mainly focused in flow patterns identification on natural circulation systems. Similar study was applied to neutron imaging data (Sunde et al., 2005). Neural networks were used to model and classify flow types using shadow subtraction and Wavelet preprocessing. Wavelet preprocessing was mentioned not to have improved results accuracy, but to have presented a positive impact on reducing neural network training time.

Methods that integrate two or more computational techniques have been used in reactor thermal-hydraulic and reactor passive safety systems (Zhang et al., 2017) and areas as medical or biological. Elsalamony (2016), makes use of the integration of image processing and pattern recognition techniques for identification and diagnosis of anemia from microscopic digital images of blood samples (swabs).

A comparison of the performance of 68 void fraction correlations to predict void fraction based on unbiased data set (2845 data points from the literature) covering vertical, inclined and horizontal two-phase flow, was performed by Woldesemayat and Ghajar (2007). Four void fraction correlation models were compared based on a total of 403 vertical flow points. Although there was a difference (of the order of 5%) between two specific correlations, in general, the comparison showed errors of the order of $\pm 15\%$, (Woldesemayat and Ghajar, 2007). These discrepancies call attention to the need of more experimental studies in order to validate void fraction correlation models.

Although obtaining void fraction from direct imaging implies lower cost, the method has presented intrinsic inaccuracies. Therefore, an important contribution in the current research involving two-phase flow is the identification of the factors that contribute to these inaccuracies. This effort is especially relevant when combined with the study and development of integrated image processing techniques and

intelligent algorithms. New comprehension may arise over natural circulation phenomena. The previously presented studies highlight the importance to develop integrated models involving image processing together with experimental techniques to study the behavior of two-phase flow patterns in natural circulation.

This article arises within this context and with the general aim to develop a computational system to evaluate the void fraction of natural circulation circuits using two-phase flow direct imaging. This system is composed of different integrated modules using artificial intelligence techniques with complementary and specific tasks: a) evaluation of volumetric dimensions of imaged samples taking into account the cylindrical refractions involved in image acquisition; b) segmentation based on focus metric values evaluated over the acquired images using features of acquisition depth-of-field values; c) recognition of objects-of-interest (bubbles) inside sampled images; d) finding the best association of geometrical parameters (circumference or ellipse) with the external gas-liquid interface of the detected bubbles on acquired images.

Bubble-recognition quality is one of the main features of the developed methodology. Segmentation is based on fuzzy inference. Recognition task uses a set of artificial neural networks (ANNs) trained with images sized according to the pattern to be recognized. The artificial neural networks set is integrated with a modified Hough transform to scan images with size-variable mask. Integration between the Artificial Neural Network set and the modified Hough Transform provides robustness to bubble recognition. This method was called Randomized Hough Transform with Neural Network (RHTN). RHTN yield a small number of recognized bubbles inside the selected image, avoiding the usual false recognition of a coordinates' center when only the modified Randomized Hough Transform is used.

All modules converge to evaluate void fraction at the end. Methodology is mainly based on direct imaging and adjusted using experimental gravimetric measurements (Fig. 1).

The segmentation disregards bubbles which are "out of focus" by

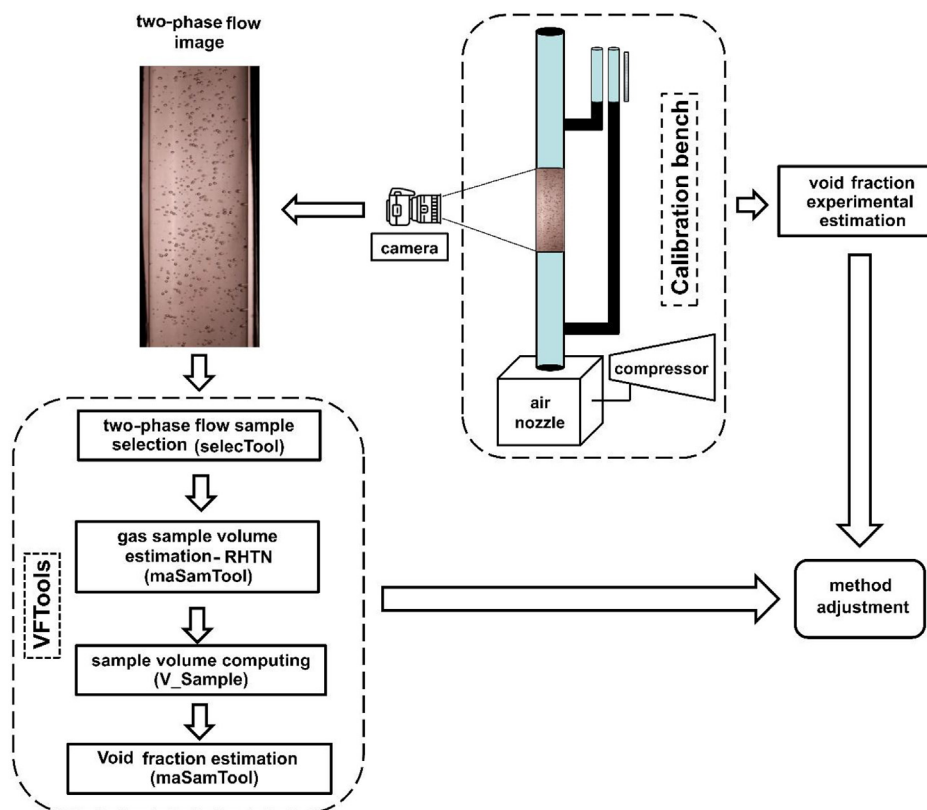


Fig. 1. Diagram of void fraction estimation system adjusted with experimental gravimetric measurements.

adjusting fuzzy inference of focus metric values. Image acquisition was appropriately set with required depth-of-field to make the bubbles localized at the background to be “out of focus”. A similar procedure was used by Zabulis et al. (2007) to detect wet foam circles from images. The cylindrical shaped tubes reinforce the need for focus depth selection, making image sampling and segmentation processes more conservative. Successive and integrated scans using RHTN are applied to detect and evaluate bubble sizes and corresponding volumes.

The void fraction estimation through direct imaging is based on image acquisition using controlled depth-of-field. These images were obtained using a two-phase vertical flow experiment using air injection, where void fraction was directly measured using a u-tube manometer. Finally, the estimations were compared with the experimental results. These experiments were done at a calibration bench of a natural circulation circuit.

These experiments were done at Nuclear Engineering Center (CEN) of the Instituto de Pesquisas Energéticas e Nucleares (IPEN) (De Mesquita et al., 2012).

2. Intelligent system

The developed computational system, named VFTools (Void

Fraction Tools) (Fig. 1), is composed of four diverse tasks where some are performed by integrated artificial intelligence techniques. These tasks are illustrated in Fig. 2.

The first three blocks at upper side of Fig. 2, show the focus-based fuzzy segmentation task. Input flow image is shown in horizontal position though the flow is upward. The original acquired images are stored in RGB system files to be analyzed. They are converted to normalized grayscale system before the fuzzy inference. The second line on diagram shows other interlinked three blocks which represent the bubble detection and recognition task. This task is performed by successive scans using masks with controlled sizes. In the third line of Fig. 2, more three blocks are represented. These interlinked blocks show the volume evaluation based on a detected bubble of previous task. This evaluation is based on estimated geometrical parameters of an ellipse or circumference shape, which is chosen to correspond with detected bubble. The total gas (air or water vapor) volume of the imaged flow sample is evaluated taking into consideration some homogeneity hypotheses. First, the bubble-density homogeneity over the transversal plane and longitudinal length. The volumetric (three-dimensional) homogeneous extension of the bubble bidimensional image is also an important hypothesis. Finally, in the fourth line of Fig. 2, the three interlinked blocks show the void fraction calculation as the ratio

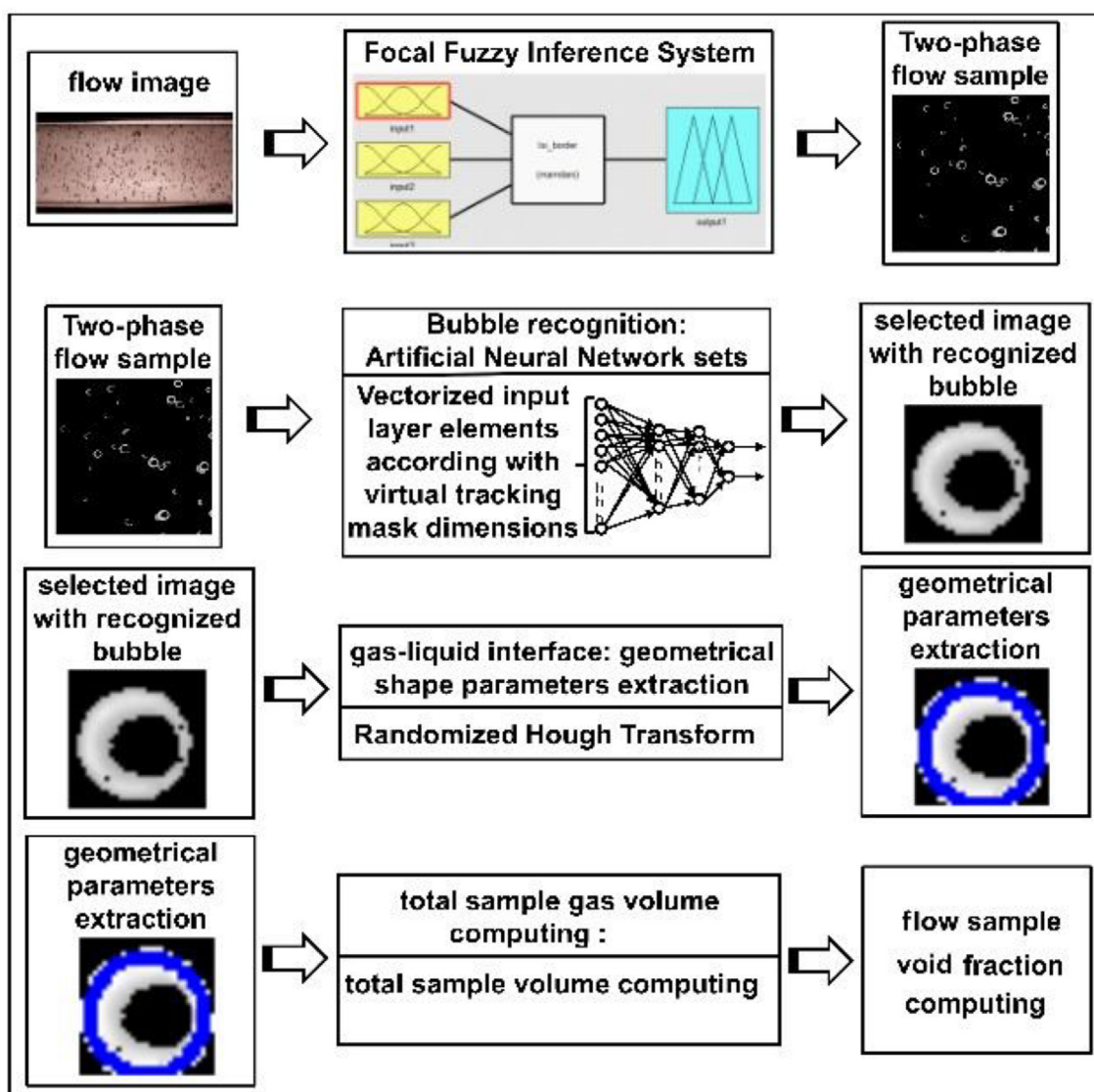


Fig. 2. VFTools main tasks block diagram.

between the total gas volume and the whole imaged flow volume. Total gas volume estimation is the summation of individual estimated bubble volumes. Appropriate calibration is used to relate the local void fraction with void fraction measurements of the whole experimental circuit.

2.1. Natural circulation phenomenon and image acquisition

Flow patterns are determinant to identify specific heat transfer boundary conditions of the natural circulation phenomenon. This phenomenon is mainly due to driving forces caused by circulating coolant density variations (Hsieh et al., 1997).

Thermal stability in two-phase natural circulation systems assumes that flow rate is dependent on the void amount generated due to heat addition and pressure drop. Void fraction estimation as well as frictional pressure drop are key parameters for predicting instability threshold for those systems (Nayak et al., 2007). Void fraction usually can be considered as having influence on these systems' stability boundaries.

2.2. Flow sample selection

In this work, Focal Fuzzy Inference System (FFIS) is used to select image samples of captured image. The input images were originally captured in color mode. The three color-channels were converted to one normalized gray intensity channel as color information has shown low impact on pattern recognition tasks.

The sampling task had two main goals: to choose the image area where refraction (Masotti and Mesquita, 2015) is reduced, and obtain image blocks which would be faster to be processed in the subsequent phases of the system. The chosen sampling used an 800×800 pixels' image size.

The image sample depth estimation is done using the FFIS. This system uses traditional focus metric (Krotkov, 1987) to create fuzzy membership functions and rules to infer what objects (bubbles), in image, are in focus. The images were acquired with predefined depth-of-field. The experimental depth-of-field value will further be used to calculate the corresponding sample volume. The fuzzy inference is done for each pixel, based on three different inputs: the first input is the normalized gray level intensity, the second input is the normalized sum of the negative gray level intensity added to the first derivative of gray level intensity (obtained by Sobel operator) and the third input is the normalized sum of the negative-gray level intensity with the second derivative of gray level intensity (obtained by Laplacian operator). In Fig. 3 the schematic representation of the FFIS over a typical flow image is illustrated. Determination of the area-of-interest in sampling process is done before FFIS inputting. Each fuzzy input feature is evaluated for each pixel. For each operation as Sobel, or Laplacian application a corresponding matrix is obtained. The inputs are obtained by adding up these matrices directly. Each pixel is classified as "in-focus" or "out-of-focus". The membership functions were constructed based on statistical studies over bubble-boundaries' profiles.

Statistical studies were done using bubble images previously classified as *in-focus* or *out-of-focus*. These profiles were selected from each sampled bubble. A typical boundary profile selection is shown by a white line as illustrated in Fig. 4. These statistical studies are better described in Section 6.1.

2.3. Bubble recognition and volume calculation

The second phase of the system is composed of two tasks previously described (Fig. 1) as flow sample selection and sample volume estimation. This phase can be summed up as firstly detect the bubbles inside each image sample and for each bubble, evaluate its volume. After this is repeated for all detected bubbles, the total gas volume is calculated. The input for this phase, is an image which contains many 'in-focus' bubbles. Estimated volume summation of detected bubbles inside

the sampled image represents the total gas (air or water vapor) volume. This value is important for void fraction calculation.

Each detected bubble volume is added in a cumulative variable that

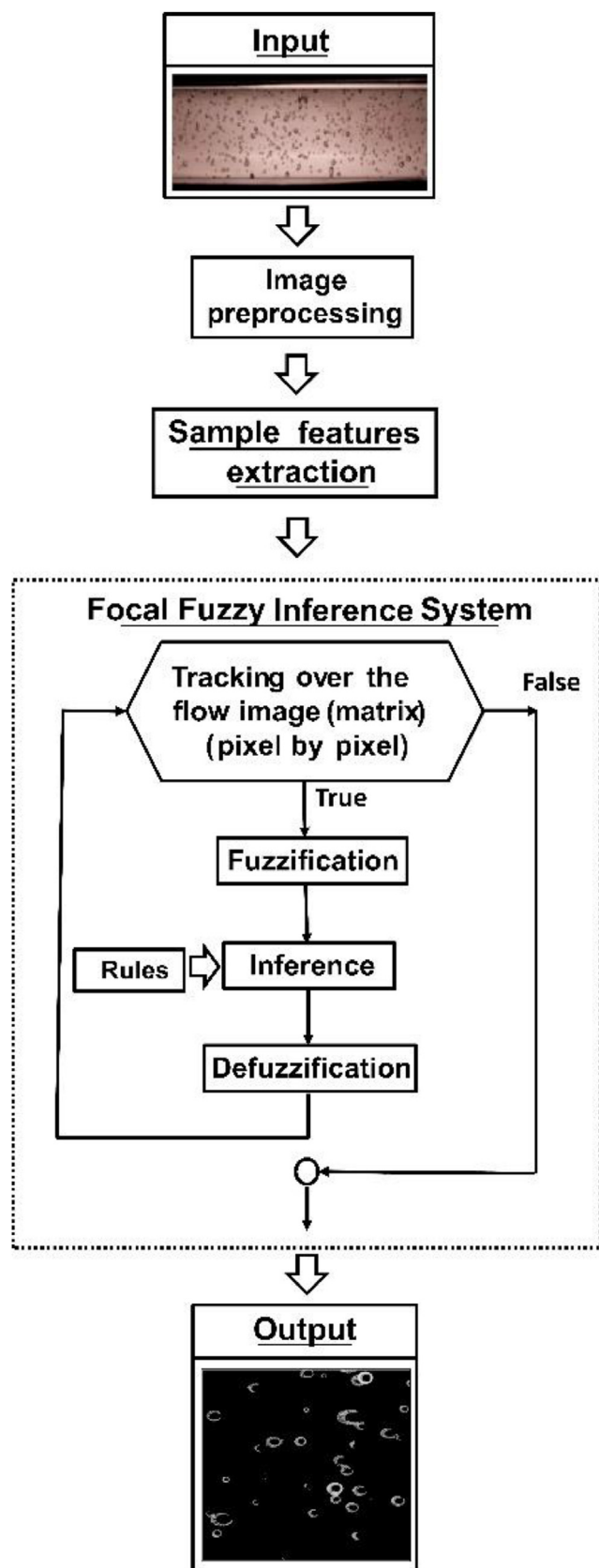


Fig. 3. Focal fuzzy inference system.

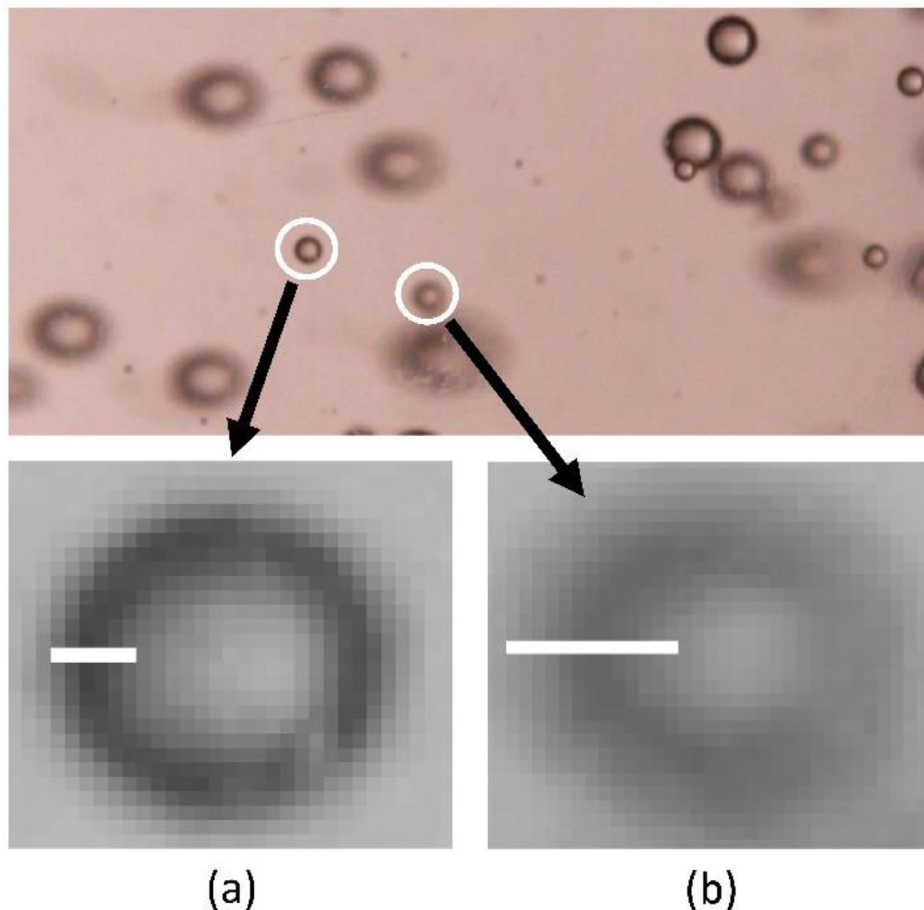


Fig. 4. (a) *in-focus* and (b) *out-of-focus* boundary bubble profiles from two-phase flow image.

is updated every time a new detection occurs. The detected bubble is then erased from sampled image. The cumulative variable content (bubbles' volume summation) is, after all bubble images are detected, the estimated total gas (air or water vapor) volume of the two-phase flow sampled image.

The use of masks with progressive and controlled dimensions is a novel pattern detection method. These dimension-controlled masks are applied through image convolution, step-by-step, selecting small parts of the image. The convolution process starts with a square mask sized with the smaller bubble image dimensions. It is performed, pixel by pixel, over all sampled image. The mask size is increased after the first image scan is complete in order to initiate the next scan. This cyclic and progressive scan is performed until the mask attains the size of the largest bubble image.

The progressive mask covers small parts of the image with pixel by pixel displacement. After each displacement, an Artificial Neural Network (ANN), previously trained to recognize bubbles with compatible sizes, is applied in order to output the presence (or not) of a bubble inside the mask. In case of no bubble's recognition (negative case), the mask is displaced again by one pixel over the sampled image, and a new part of image is submitted to the ANN recognition process. In case of a bubble detection, the bubble image border is submitted to a geometrical shape identification process. This process is based on the Randomized Hough Transform technique that searches for appropriate association of an analytical geometrical figure (ellipse or circumference) to a set of randomly selected pixels. In this work, the random pixel selection is performed over the external border of detected image, which is considered as the gas-liquid interface. The bubble volume is computed based on RHT obtained geometrical parameters. After the bubble volume is obtained, the bubble image is erased from sampled image to

avoid its double recognition.

A block diagram of RHTN method is illustrated in Fig. 5. The method is the association of Feedforward Multilayer Perceptron Artificial Neural Networks with a modified Randomized Hough Transform to detect and dimension bubbles inside a sampled image. RHTN ensures an accurate and robust estimation of detected bubble dimensions. The total gas volume in the sampled image can be computed through these dimensions' estimation. The RHTN is designed to: a) avoid the possible loss of consistency in RHT results when false bubbles are detected (false positive) by ANN and b) to restrict the classification of border pixels as pertaining to a "bubble" only if, at least 55% of them, can be contained within an analytical shape inside mask dimensions. This last condition was established in order to avoid considering two bubbles as one, when occlusion happens.

In this work, the ANN input layer receives the normalized gray intensity values of the selected flow image pixels. The ANN output layer uses binary coding to represent positive detection ([1,0]). The initial ANN input layer has 901 neurons corresponding to the initial mask size (30 by 30 pixels). The extra element is called independent element, or bias, used to adjust the ANN activation function. The initial mask size is defined based on the smallest bubble dimension in flow sampled images. This value is established as consequence of a quantitative analysis using 192 image samples. Each new mask size is followed by the addition of a new input ANN layer, and a new training is done to update the ANN weights. This iterative process is performed until the mask size is enough to recognize the largest bubbles in sample images.

The ANN training (Fig. 6) is performed using extracted image samples with increasing controlled dimensions as input. Training data file contains approximately 4500 images of different sizes and their corresponding output labels. This data file is manually created by

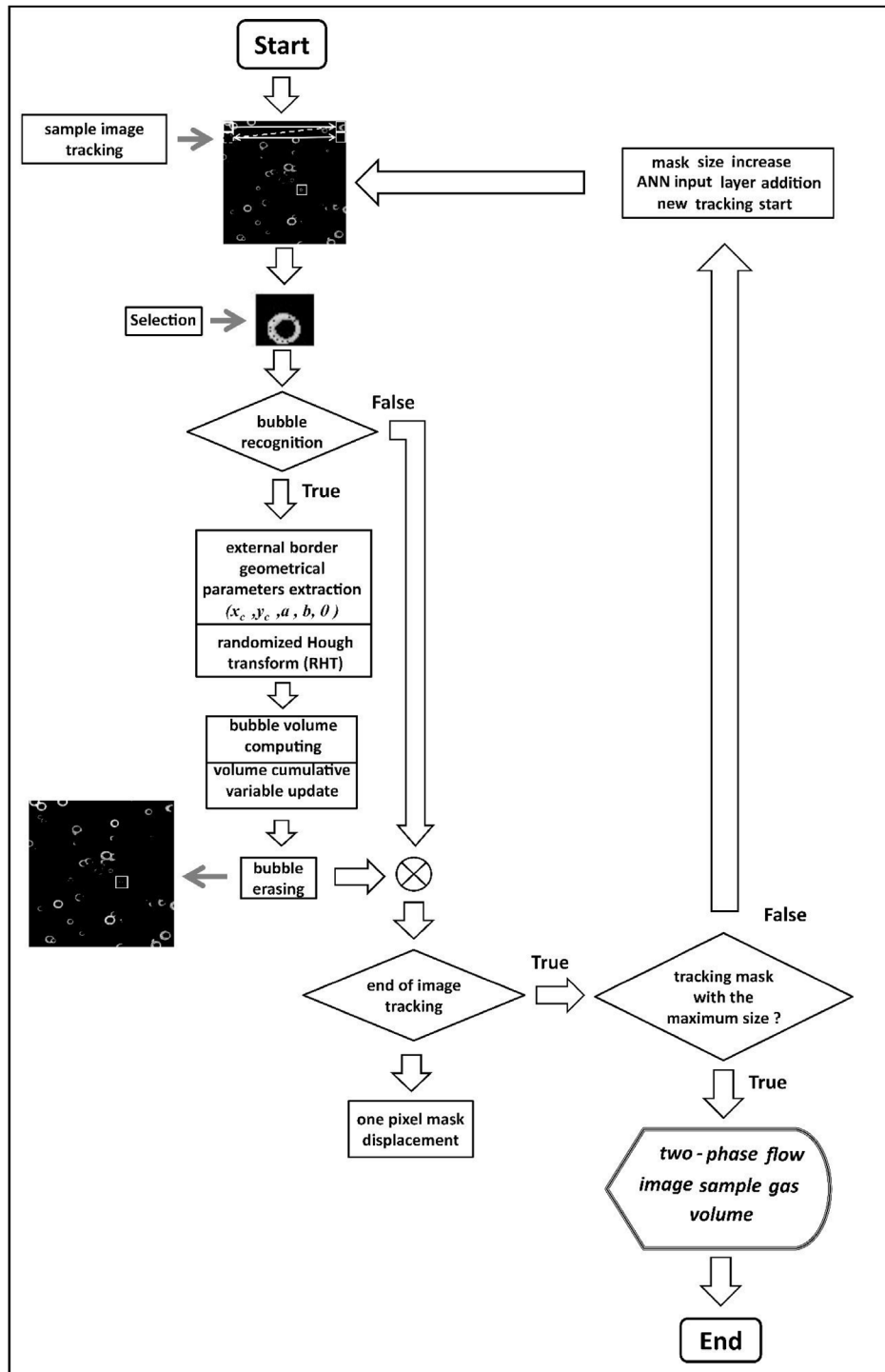


Fig. 5. Randomized Hough Transform with Neural Network (RHTN) algorithm.

labelling positive and negative detection of bubbles in image samples. Positive detection is labelled when: a) a whole bubble is contained by image of the detection controlled-mask or b) there is at least one empty line or column between the bubble border and the mask boundary. Another condition is also considered as positive recognition: the presence of a set of bubble border pixels inside the mask and the presence of the remaining part of an occluded bubble which was partially erased on a previous scan. Negative labelled recognition is characterized by: a) complete absence of bubbles inside the image mask boundaries or b) bubbles with border over more than one mask boundaries or c) remains of erased bubbles by prior scanning or d) incomplete bubbles inside the

mask or e) bubbles which are significantly larger than the mask dimensions.

Four to five thousand of samples are selected to build a training file corresponding to each mask size. ANN training uses Conjugate Gradient Method to error minimization through weights update. Each selected mask size generates a set of synaptic weights. These synaptic weight sets compound the ANN knowledge basis for bubble recognition tasks.

2.4. Two-phase flow void fraction estimation

Previous tasks provide values to estimate the void fraction of the

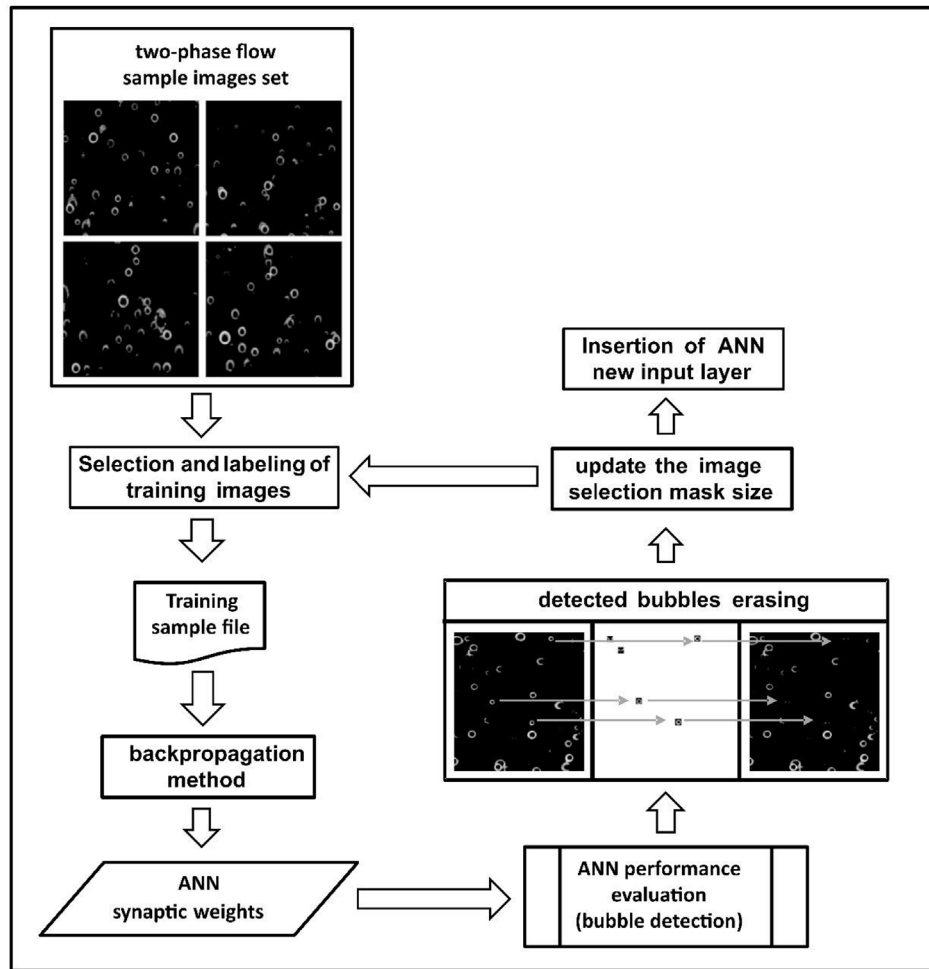


Fig. 6. ANN progressive training sequence.

sampled image. These volume values for each bubble are stored on a cumulative variable in order to estimate total gas (air or water vapor) volume inside the imaged cylindrical tube section. The flow sample total volume is the volume of this section. The void fraction can be estimated by the ratio between these two values as:

$$\alpha = \frac{\text{Gas total volume in the flow sample}}{\text{Flow sample total volume}} \quad (2.1)$$

3. Artificial intelligence techniques and Hough Transform

Fuzzy Logic, Artificial Neural Network and Randomized Hough Transform were the main techniques used to develop the void fraction

estimation system (VFTools). This system can be applied to two-phase flow images of natural circulation circuits, specially involving cylindrical geometry refraction on acquisition conditions.

3.1. Fuzzy inference system (FIS) for segmentation threshold estimation

The image segmentation threshold for determining *in-focus* bubbles was estimated by a Focal Fuzzy Inference System (FFIS) that used three focus quality variables as input (Krotkov, 1987). Based on this inference, the image sample depth can be considered as the experimental depth-of-field used for acquisition. More detailed description are shown in section 4.

A Fuzzy Inference System is a logical system that estimates “true”

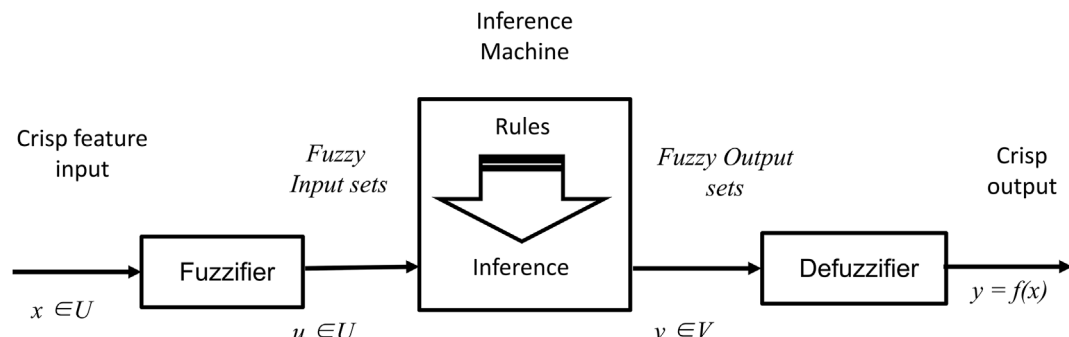


Fig. 7. Fuzzy inference system (FIS).

values for its sentences inside a continuous [0,1] interval. There is an inference machine that does a composition of a set of logical sentences that represents the knowledge base. The inference mechanism imbeds artificial intelligence on the system. This mechanism is based on the classic set theory with an extension which allows that logical sentences can be constructed based on linguistic variables. These variables are based on membership functions that allows a numerical variable to assume different membership degrees for different linguistic variable labels.

According to Mendel (1995), a Fuzzy Logic System is a mapping of a feature input data vector (with crisp features) to a crisp scalar output data vector intermediated by an inference that uses fuzzy variable sentences. The main advantages of using fuzzy logic are the numerous alternatives to map traditional engineering variables with knowledge base of other areas. Another fuzzy advantage is the simplification of these computational mappings since it allows the use of linguistic variables. Fig. 7 shows a FIS block diagram with its main elements.

The system input is a vector with relevant feature elements. In this paper, focus metrics (Krotkov, 1987) applied to the image samples were the base for the input variables to FIS. The inference system outputs a label *in-focus* or *out-of-focus* to each image pixel.

The elements of this feature input vector are fuzzified and associated with linguistic variables through membership functions. These variables may assume different linguistic values, known as labels. Fuzzification attributes a label membership degree (0–1) for each crisp input. Membership functions are usually constructed considering expert evaluations.

The first input variable of the fuzzy inference system was the normalized gray intensity I_{xy} , which low values indicate *in-focus* image pixels was used to construct the first membership function shown in Fig. 8. The complementary gray intensity level (also called negative gray intensity), $I_{xy}^{(-)} = 1 - I_{xy}$, was used to construct the membership functions shown in Figs. 9 and 10. Fig. 9 shows the second FIS input membership functions based on Sobel operator, S_{xy} , that represents the first directional derivative of the pixel gray intensity. This variable is related to evidence of border occurrences. The third input variable was constructed based on Laplacian operator, L_{xy} . The membership functions are shown in Fig. 10. Laplacian operator is the second derivative of gray intensity and it represents a fast deviation in gray intensity, an appropriate feature for edge detection. Analysis based on these features demands caution because they can represent noise occurrences in the image. Krotkov (1987) indicated that this set of parameters, with an appropriate threshold definition, could establish a standard measure for each image pixel related to focus quality.

The FFIS inference results for each image pixel, classify the pixel as *in-focus* (therefore should be inside of acquisition depth-of-field) or *out-of-focus* (should be outside of acquisition depth-of-field). The membership functions were constructed based on statistical analysis of a set of *in-focus* (*if* subscript) and *out-of-focus* (*oof* subscript) bubble border profiles, extracted from two-phase flow image samples. The result of these analyses obtained the mean (represented with a horizontal bar

over the variable) and standard deviation of the parameter. Fig. 8 presents the gray intensity membership functions. The *in-focus* profile values were extracted from bubble border images. The gray intensity values for *in-focus* (I_{if}) of bubble profiles are close to zero (dark or black). The mean value is shown as the gray intensity average of the edge profile pixels, \bar{I}_{if} . The maximum value of *in-focus* membership function was considered to be the average of the gray intensity of the *in-focus* pixels added by one standard deviation, $\bar{I}_{if} + \sigma$. Similar considerations were made for *out-of-focus* membership function, where the minimum value for this function was defined as the average of the gray intensity subtracted by the standard deviation, $\bar{I}_{oof} - \sigma$.

Equations (3.1) and (3.2) consist of general expressions for calculating the average of any variable and its corresponding standard deviation σ , respectively:

$$\bar{m} = \frac{\sum_{i=1}^n m_i}{n} \quad (3.1)$$

$$\sigma = \sqrt{\frac{\sum_{i=1}^n (\bar{m} - m_i)^2}{n - 1}} \quad (3.2)$$

The “ n ” value corresponds to the considered number of pixels of border profile. The generic “ m_i ” is the parameter value for the “*i-pixel*” under analysis.

The fuzzy membership functions constructed based on Sobel and Laplacian operators are shown in Figs. 9 and 10. These functions used the compositions of the negative gray intensity added with the applied operators.

Fig. 10 shows the membership function for negative gray intensity added by Sobel operator application over a profile border of a bubble image, $IS_{xy} = I_{xy}^{(-)} + S_{xy}$. The mean, $\bar{IS}_{xy} = (\bar{I}_{xy}^{(-)} + S_{xy})$, and the normalized mean standard deviation values, σ , of this parameter were obtained from a statistical analysis for *in-focus* (*if* subscripts), and *out-of-focus* (*oof* subscripts) bubble images profile border samples. The same notation are adopted in Fig. 10 where, $IL_{xy} = I_{xy}^{(-)} + L_{xy}$ represents the negative gray intensity added the Laplacian operator application over a bubble image and, $\bar{IL}_{xy} = (\bar{I}_{xy}^{(-)} + L_{xy})$, its correspondent mean for *in-focus* and *out-of-focus* bubbles image profile border samples with related mean standard deviation, σ .

Fig. 11 shows the FFIS output membership functions where the classification boundary is located around half of the abscise axis.

The inference machine was done using a Mamdani inference system (Mamdani and Assilian, 1999) and was composed of eight fuzzy inference rules (Table 1) based on fuzzy variables shown in Figs. above.

The subscripts “*oof*” and “*if*” complements the meaning of the linguistic variables with the terms *out-of-focus* and *in-focus*, respectively. The expressions on Table 1 are fuzzy logical propositions that are evaluated based on each variable proposition membership value (μ). The intersection operator “ \cap ” represents the “and” Boolean operator that is implemented in FFIS using t-norm operator (Mendel, 1995).

Final classification is performed based on the estimation of which label is chosen, and what crisp value should correspond to it. This

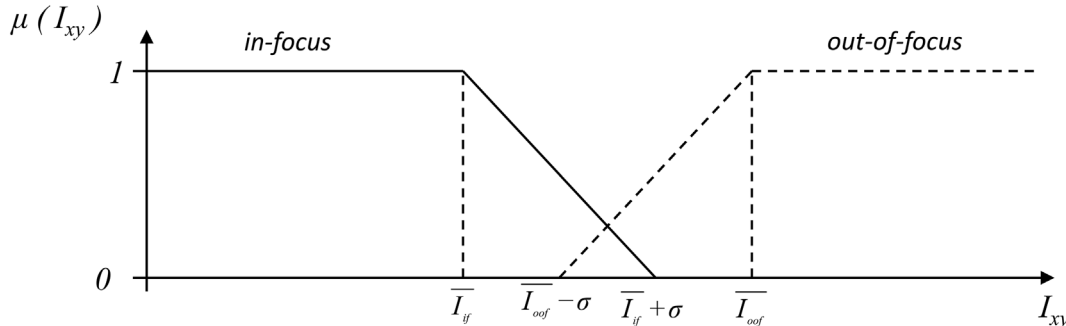


Fig. 8. Gray Intensity (I_{xy}) membership functions.

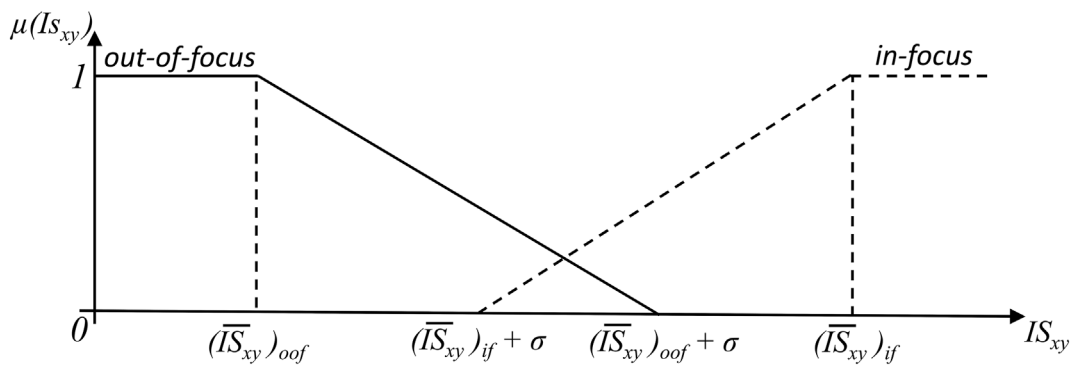


Fig. 9. Negative Gray Intensity added with Sobel (IS_{xy}) membership functions.

process is called “*defuzzification*”. The FFIS defuzzification method used was the traditional Centroid method (Mamdani and Assilian, 1999).

The classification is performed using the evaluated centroid value and can be summarized by expressions 3.4 and 3.5:

$$C_{og} \leq 0.5 \Rightarrow \text{out-of-focus pixel} \quad (3.4)$$

$$C_{og} > 0.5 \Rightarrow \text{in-focus pixel} \quad (3.5)$$

3.2. Artificial neural network for segmentation

Bubble recognition task was implemented using a set of feedforward multilayer artificial neural networks, also known as Multilayer Perceptrons.

Inspired in the biological brain processing model, Artificial Neural Networks (ANNs) are intelligent algorithms, formed by interconnected processing units known as artificial neurons. This network topography is usually organized in columns which are known as input, hidden or output layer depending on data flow order. More traditionally known as Multilayer Artificial Neural Networks are historically called Multilayer Perceptrons Networks, (Schmidhuber, 2015).

An artificial neuron represents the basic ANN design unit. Based on this model, an ANN is designed and computationally implemented, where $w_{k1}, w_{k2}, \dots, w_{km}$ are the “ k ” neuron synaptic weights, that may represent the ANN embedded knowledge after the training phase is completed. Synaptic weights usually are the free parameters that are updated based on supervised learning, where an extensive training database is used with known target correspondence between output and input vectors. The weights act over an input signal, x_1, x_2, \dots, x_m , as a multiplier. The first result of the linear combination of the input vector multiplied by the synaptic weights, “ u_k ”, added to a bias, “ b_k ”, is known as Local Induced Field, “ v_k ”. An activation function, “ $\varphi(\cdot)$ ”, is used to threshold the output value inside [0,1] interval.

The bias, b_k , is a parameter applied to displace the Local Induced Field, v_k . For convenience, the bias can be treated as another synaptic weight, w_{k0} , where its correspondent input signal, x_0 , is assumed to be

‘1’. Therefore, the artificial neuron can be expressed by equations (3.6) and (3.7).

$$v_k = \sum_{j=0}^m w_{kj} \cdot x_j \quad (3.6)$$

$$y_k = \varphi(v_k) \quad (3.7)$$

This model is conveniently used for vectorized notation adopting X as vectorized input:

$$X = [1 \ x_1 \ x_2 \ \dots \ x_m]^T \quad (3.8)$$

The vectorized synaptic weights of neuron k , considering $w_{k0} = b_k$, is expressed by equation (3.9):

$$W_k = [w_{k0} \ w_{k1} \ \dots \ w_{km}]^T \quad (3.9)$$

The output neuron, k , is obtained by equation (3.10):

$$y_k = \varphi(X \cdot W_k^T) \quad (3.10)$$

This ANN description considers a full-connected architecture where all neurons are interconnected. This architecture consists of an input layer, represented by input vector elements, a set of intermediate layers (“*hidden layers*”), each presenting many neurons and an output layer. The computation procedure for the whole network is similar to the previously described to a single artificial neuron. The input of the second layer corresponds to the output of the previous layer (Fig. 12).

The neural network input (Fig. 12) is the vector X (Equation (3.8)). The elements of the first hidden layer, $a_i^{(1)}$, are the result of the input signal X vector multiplied by the corresponding synaptic weight matrix, $W^{(0)}$, and then submitted to the activation function. The result is added to the implicit bias yielding the vector $a^{(1)}$ (Equation (3.11)) that can be used as input for the next layer.

$$a^{(1)} = [1 \ \varphi(X \cdot W^{(0)})]^T \quad (3.11)$$

The synaptic weight matrix, $W^{(0)}$, applied to input signal is expressed by equation (3.12):

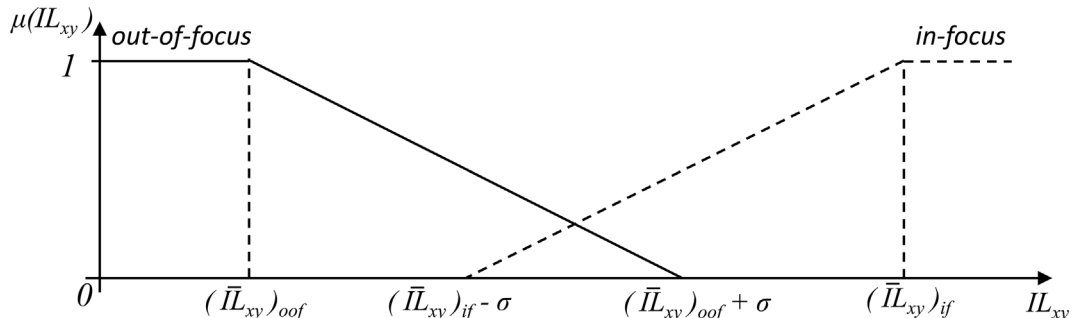


Fig. 10. Negative Gray Intensity added with Laplacian (IL_{xy}) membership functions.

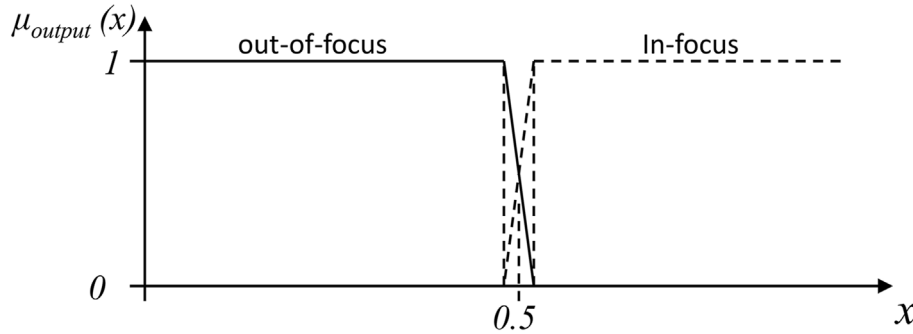


Fig. 11. Focal fuzzy inference system output membership functions.

Table 1

Rules applied in fuzzy inference systems.

#	Expression
1	$\mu(I_{xy})_{oof} \cap \mu(IS_{xy})_{oof} \cap \mu(IL_{xy})_{oof} \Rightarrow (\mu_{output})_{oof}$
2	$\mu(I_{xy})_{oof} \cap \mu(IS_{xy})_{oof} \cap \mu(IL_{xy})_{if} \Rightarrow (\mu_{output})_{oof}$
3	$\mu(I_{xy})_{oof} \cap \mu(IS_{xy})_{if} \cap \mu(IL_{xy})_{oof} \Rightarrow (\mu_{output})_{oof}$
4	$\mu(I_{xy})_{oof} \cap \mu(IS_{xy})_{if} \cap \mu(IL_{xy})_{if} \Rightarrow (\mu_{output})_{if}$
5	$\mu(I_{xy})_{if} \cap \mu(IS_{xy})_{oof} \cap \mu(IL_{xy})_{oof} \Rightarrow (\mu_{output})_{if}$
6	$\mu(I_{xy})_{if} \cap \mu(IS_{xy})_{oof} \cap \mu(IL_{xy})_{if} \Rightarrow (\mu_{output})_{if}$
7	$\mu(I_{xy})_{if} \cap \mu(IS_{xy})_{if} \cap \mu(IL_{xy})_{oof} \Rightarrow (\mu_{output})_{if}$
8	$\mu(I_{xy})_{if} \cap \mu(IS_{xy})_{if} \cap \mu(IL_{xy})_{if} \Rightarrow (\mu_{output})_{if}$

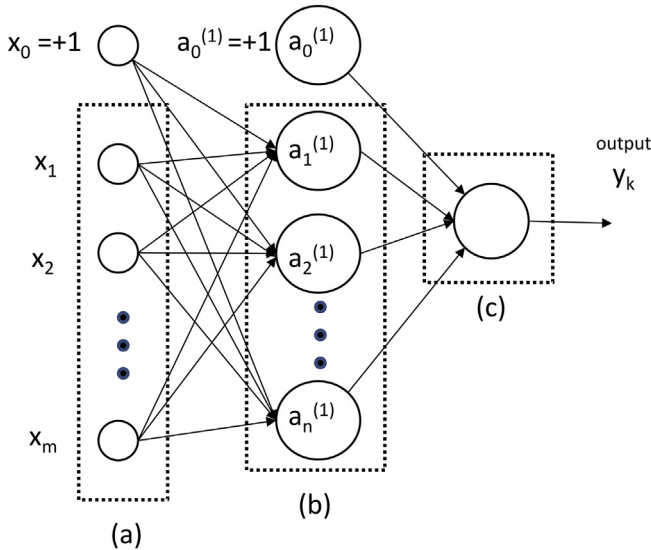


Fig. 12. Multilayer Perceptron: (a) input layer; (b) hidden layer; (c) output layer.

$$W^{(0)} = \begin{bmatrix} w_{0,0}^{(0)} & \dots & w_{0,n}^{(0)} \\ \vdots & \ddots & \vdots \\ w_{m,0}^{(0)} & \dots & w_{m,n}^{(0)} \end{bmatrix} \quad (3.12)$$

The final ANN output, y_k , is:

$$y_k = \varphi(a^{(1)^T} \cdot W^{(1)}) \quad (3.13)$$

 $W^{(1)}$ is the synaptic weight matrix of the hidden-output layer.

Synaptic-weight matrices are the most common parameters updated during an ANN training process. Backpropagation algorithms are the most used techniques for this training process. The ANN free parameters are updated based on the output average error for each input-

output pair used on a supervised training.

Coates et al. (2011) and Wang et al. (2012a,b) uses a conjugate gradient algorithm to obtain the minimum cost function related to synaptic weights, " J_W ". At this condition, the training is finished, and the synaptic weights are finally updated. The cost function consists of the average error by submitting all labelled samples to ANN.

3.3. Randomized Hough Transform (RHT) for bubble geometrical estimation

The geometrical properties of recognized bubbles are important to estimate void fraction. Yip et al. (1992) recognized that Hough transform is a robust technique to estimate analytical shapes in an image. Its conventional use is achieved in two steps. Firstly, through a voting rule, a cumulative matrix is incremented based in a transformation mapping. Finally, an exhaustive search process over the cumulative matrix occurs, looking for candidate shapes that corresponds to target parameters, and then, a validation is done. This transform requires a cumulative matrix with five dimensions (center of coordinates, minor and major semi axes and inclination angle).

Conventional Hough-transform algorithm time and memory computational space grow up exponentially with the number of parameters in cumulative matrix. Tsuji and Matsumoto (1978), Davies (1987) and Nixon (1990), developed modified Hough transform algorithms with the purpose to improve computational performance. Although they had performance improvements, some results got worse at some specific conditions.

Yip et al. (1992) developed a modified Hough transform with reduced computational memory requirements, keeping robustness and efficacy. This model showed good results when applied in well-defined analytic shapes. However, when used in experimental two-phase flow patterns, where bubble boundaries present irregularities or may present occlusions, the model did not apply.

The Randomized Hough Transform algorithm developed by Yu et al. (2008) presented expressive reduction of the number of elements in cumulative matrix, resulting in better performance. They also could detect occluded ellipses using their method.

Teng (2012) and Zhang et al. (2012) described several applications of Hough Transform models evidencing their potentialities. Zhang et al. (2012) used Randomized Hough Transform applied to dispersed bubbles in two-phase flow.

McLaughlin (2000, 1998) pointed that RHT is the adequate model to be applied in images with small number of ellipses or circumferences. RHT presented the best performances in these cases. In general, a border detection operator is required to estimate the geometry and dimensions of objects-of-interest inside images. Usually this detector will provide pixel candidates for RHT to identify the border shape (ellipse or circumference).

In this paper, declivity methods were discarded. Although they are usually indicated as border detectors (Bhardwaj and Mittal, 2012), they require a prior knowledge of the intensity of pixels around the border to

be detected. RHTN has an important feature that uses different mask sizes to scan whole image. The use of the dimension-controlled mask in the present work, restricts this data to be inside its boundaries. The Canny operator showed to be a better option (Bhardwaj and Mittal, 2012) for this task. This detector additionally provides the pixel derivatives that represent the angular coefficients of the line that is tangent to the candidate border. The present work can estimate partially occluded ellipses.

RHT uses a coordinate axis with origin at upper left corner of the image. The row and column coordinates were identified by "r" and "c" subscripts. The method starts with random selection of candidate pixels to a shape border. Their coordinates are combined as a uniform probability distribution.

These bubble-border pixel coordinates (c_b, r_b), and their directional derivatives were obtained by a Canny detector application. The sample size was defined as fifty five percent of the total number of combinations of pixels' coordinates. The directional derivatives of these pixels are indicated by $g_y(c_b^{(i)}, r_b^{(i)})$ and $g_x(c_b^{(i)}, r_b^{(i)})$, where the superscript "i" vary from "1" to the mask size, "s". These derivatives are used to obtain the angular coefficient of the supposed border point tangent, m_t^i . The correspondent tangent line linear coefficient, " $b_t^{(i)}$ " is obtained for each candidate coordinate. The ellipse (or circumference) center is in the line that passes over the intersection point of two distinct tangent lines ($c_t^{(i,j)}, r_t^{(i,j)}$), and its medium point coordinates ($c_m^{(i,j)}, r_m^{(i,j)}$). Angular and linear coefficients, $m_c^{(i,j)}$ and $b_c^{(i,j)}$, respectively, for each pair of border points, could be obtained:

$$m_c^{(i,j)} = \frac{r_t^{(i,j)} - r_m^{(i,j)}}{c_t^{(i,j)} - c_m^{(i,j)}} \quad (3.17)$$

$$b_c^{(i,j)} = r_m^{(i,j)} - m_c^{(i,j)} \cdot c_m^{(i,j)} \quad (3.18)$$

The RHT theoretical fundamentals (shown in Fig. 13) can be written in the reduced-form line (L) equation:

$$r_{sc} = m_c^{(i,j)} \cdot c_{sc} + b_c^{(i,j)} \text{ for } c_{sc} = 1, \dots, s \quad (3.19)$$

Where " $L(c_{sc}, r_{sc})$ " represents each candidate line that could pass through the shape center.

For each coordinate computed over these generated center lines, a vote is added to a cumulative matrix. The center of the shape, " $C(c_c, r_c)$ ", is chosen based on the greater number of votes. This estimation may present some uncertainty due the random pixel-pairs selection and the presence of small differences between neighbor coordinates.

In this work, some modifications were developed to improve the fitting between the chosen shape and the set of pixels. Firstly, the four most promising shape-center candidates are selected based on the following condition: only are considered to this group if their voting differs by less than or equal to two votes and if they are localized with distance smaller than two pixels. Ellipsoid parameters will be evaluated for this group to choose the best option.

The other ellipse parameters are independently estimated: major semi axis, " a ", minor semi axis, " b ", and inclination angle, " θ ", between the major semi axis to the local horizontal axis (Fig. 14). The estimation of these parameters requires translation of selected pixels from image coordinate system to the ellipse-center coordinate system, " $O (0,0)$ " (Fig. 14) as equations (3.20) and (3.21) shows:

$$c_O^{(i)} = c^{(i)} - c_c \quad i = 1, 2, \dots, s \quad (3.20)$$

$$r_O^{(i)} = r^{(i)} - r_c \quad i = 1, 2, \dots, s \quad (3.21)$$

Selected border-pixel candidates are reorganized in triples indexed as $i = 1, 2, \dots, s; j = 1, 2, \dots, s (j \neq i)$ and $k = 1, 2, \dots, s (k \neq j \neq i)$. That is the minimum required number of parameters to analytically establish an ellipse. The general equation is then expressed by:

$$A. (c_O^{(i)})^2 + B. (c_O^{(i)}) \cdot (r_O^{(i)}) + C. (r_O^{(i)})^2 = 1, \quad (3.22)$$

where:

$$A = \frac{\cos^2\theta}{a^2} + \frac{\sin^2\theta}{b^2} \quad (3.23)$$

$$B = 2 \cdot \left(\frac{1}{a^2} - \frac{1}{b^2} \right) \cdot \sin \theta \cdot \cos \theta \quad (3.24)$$

$$C = \frac{\sin^2\theta}{a^2} + \frac{\cos^2\theta}{b^2} \quad (3.25)$$

A linear system may be constructed base on the selected triple as:

$$\begin{bmatrix} A \\ B \\ C \end{bmatrix} = \begin{bmatrix} (c_O^{(i)})^2 & c_O^{(i)} r_O^{(i)} & (r_O^{(i)})^2 \\ (c_O^{(j)})^2 & c_O^{(j)} r_O^{(j)} & (r_O^{(j)})^2 \\ (c_O^{(k)})^2 & c_O^{(k)} r_O^{(k)} & (r_O^{(k)})^2 \end{bmatrix}^{-1} \cdot \begin{bmatrix} 1 \\ 1 \\ 1 \end{bmatrix} \quad (3.26)$$

The linear system solution are the A , B and C values that allows the estimation of the ellipse geometrical parameters since the inequality (3.42) be true:

$$A \cdot C - \left(\frac{B}{2} \right)^2 > 0 \quad (3.27)$$

Ellipse geometrical parameters, related to the selected border-pixel triple candidates are obtained by equations (3.28), (3.29) and (3.30):

$$b^2 = \frac{2}{A + C + \sqrt{(A - C)^2 + B^2}} \quad (3.28)$$

$$a^2 = \frac{1}{A + C - \frac{1}{b^2}} \quad (3.29)$$

$$\theta = \begin{cases} \arccos\left(\sqrt{\frac{a^2 \cdot b^2 \cdot A - a^2}{b^2 - a^2}}\right) & B \leq 0 \\ \arccos\left(-\sqrt{\frac{a^2 \cdot b^2 \cdot A - a^2}{b^2 - a^2}}\right) & B > 0 \end{cases} \quad (3.30)$$

where " $a = b$ " occurrence represents the circumference case, for which equation (3.30) don't apply and the inclination angle θ is assumed to be equal to zero.

The ellipse geometrical parameters' evaluation is a complex voting process that uses these sets of three parameters (a, b, θ) evaluated for all triples of the large sample formed by the border candidates. To choose the best fitting shape which represents the gas-liquid interface, a scan process over the cumulative matrix is done to identify the most voted triple (a, b, θ). This process is finished when this triple is evaluated for each of the group of four best candidates. The reversal process is made

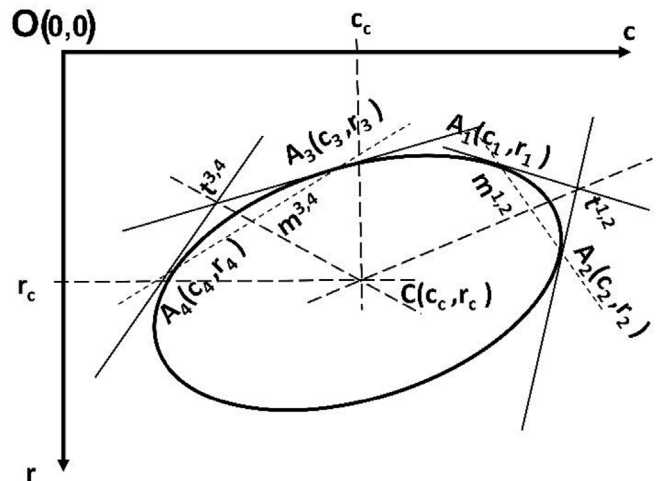


Fig. 13. Randomized Hough transform (RHT) center of ellipse or circumference method.

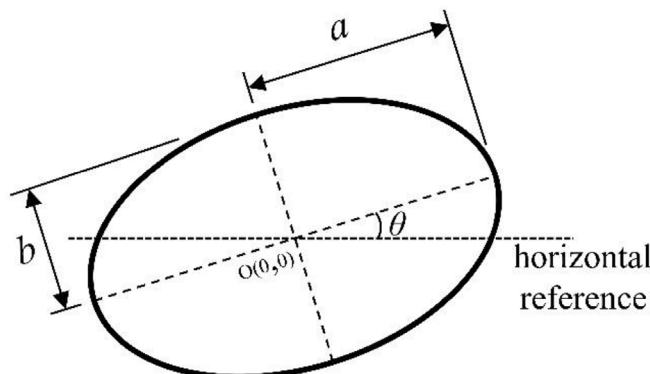


Fig. 14. Ellipse geometrical parameters.

by computing the four corresponding analytical ellipses and translating them to the image reference. Each of these ellipses are compared with the unique set of previously detected border pixels' coordinates. The ellipse with more coincident points will be chosen as the more appropriate.

After this selection, an additional criterion is imposed. The chosen ellipse should present a minimum of 55% coincidence rate in above comparison. This threshold provides an extra robustness to the overall detection performance of the system. This procedure enables a good ability to capture the geometric parameters' estimation of occluded bubbles.

A sequence of successive steps of estimating the bubble center and erasing the correctly detected pixels is done. Each sequence of erasure and estimation is done in order to verify if the internal border represents an occluded bubble or a shadow inside the bubble. An example of this process is presented in section 6.2.1.1.

4. Experimental setup

Experimental circuits with cylindrical glass tubes or visualization sections allow direct imaging using high resolution cameras. This technology may improve the quality of the obtainment of flow parameters (flow velocity, void fraction, etc.) through direct imaging. This work uses an image database with 1038 RGB image files. Image acquisition was done using a Canon EOS 5D Mark II camera where captured images of 5616×3744 pixels represented for the experiments a 50 pixels/mm resolution. Other acquisition parameters were: 0.8 ms shutter speed, ISO 6400 sensibility and 35 mm focal length under continuous backlight illumination. VFTools was designed to estimate void fraction using two-phase flow images captured in cylindrical tubes.

The void-fraction estimation adjustments were done using an experimental calibration bench with similar visualization features of the Natural Circulation Circuit (CCN) (De Mesquita et al., 2012). The experiments were done on a calibration bench which is an open-air circuit. Therefore, the pressure of the experiment was atmospheric pressure. The temperature during the experiments was ambient temperature (20–25 °C). The air injection rate was adjusted in order to obtain bubbles within 0.4 mm to 2 mm diameter size range. The calibration bench is a vertical open circuit with pressure tap points in two different heights.

A general schematic view of the calibration bench is shown in Fig. 15 and its parts are shown in the same figure as u-tube manometers, image capture section, upper circuit pressure tap and gas injection unit (air nozzle) with the lower circuit pressure tap. The measured difference between upper and lower taps' pressures is the base value for circuit void fraction measurement. This experimental value can be a benchmark for VFTools adjustments. The visualization section is a longitudinal part of the vertical glass cylindrical tube filled with water and gas injected (by an air nozzle) at its bottom.

The tube surface area to be imaged was established based on minimizing cylindrical distortion due to refraction effects. The usual limiting field-of-view angle of 10° was used to acquisition setup. This angle, δ (Fig. 16), refers to the triangle vertex at the camera sensor center formed by the field-of-view lateral borders.

The pressure of injected air could be correlated with flow rate and bubble sizes. However, for the estimation of the void fraction, the bubbles were imaged at the center of the height of the tube. It is known that bubbles near the input nozzle are smaller (higher pressure due the liquid column) and at the top of the tube are larger. The images were taken considering an average size.

Experimental depth-of-field was adjusted and controlled using a graduated focus scale beside the tube (Fig. 16).

These measurements are done while images are captured, and the estimations are synchronized in time. Two-phase flow images are captured from longitudinal circuit view section. These images are used as computational system input. Computational system adjustments and calibrations are based on comparing computed void fraction for several images of the tube section with the experimental values obtained for the whole tube.

4.1. Void fraction measurement by gravimetric method

Experimental two-phase void fraction gravimetric method can be applied in calibration bench if: a) vertical flow has very low liquid velocity; b) the gas phase is only composed of bubbles and c) the axial bubble distribution has low variation along L (small L and low friction loss). In these conditions, the average void fraction in the longitudinal section ($\langle\alpha\rangle$) is approximately the same as volumetric void fraction ($\langle\alpha\rangle_3$): $\langle\alpha\rangle \approx \langle\alpha\rangle_3$.

The pressure difference in calibration bench is captured by the water level difference, "h", between upper and lower taps shown in u-tube manometer. The pressure difference, ΔP_0 , results from gas (air) concentration between the two pressure taps' heights due to the pressure gradient arising from the mixture friction:

$$\Delta P_0 = (\rho_m g L + \Delta P_t) - \rho_L g L \quad (4.1)$$

Where ρ_m is the gas-liquid mixture density (in kg/m³); ρ_L is the liquid

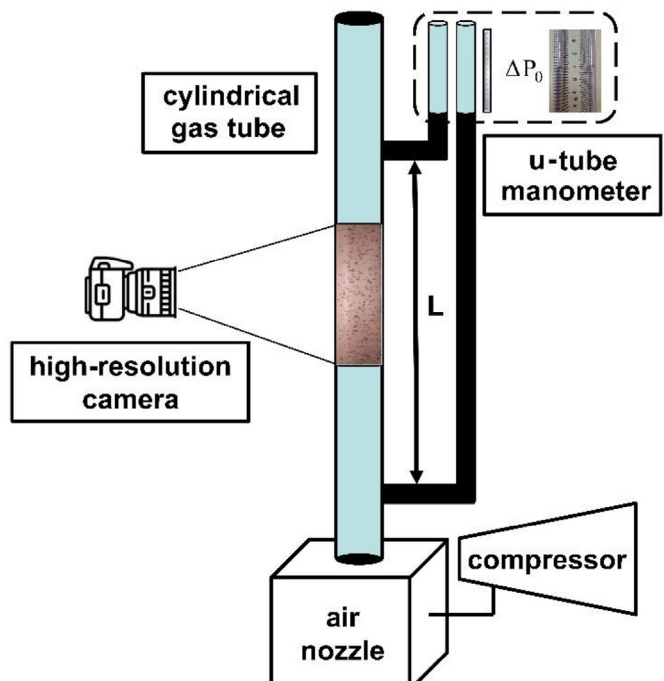


Fig. 15. Schematic presentation of the void fraction calibration bench.

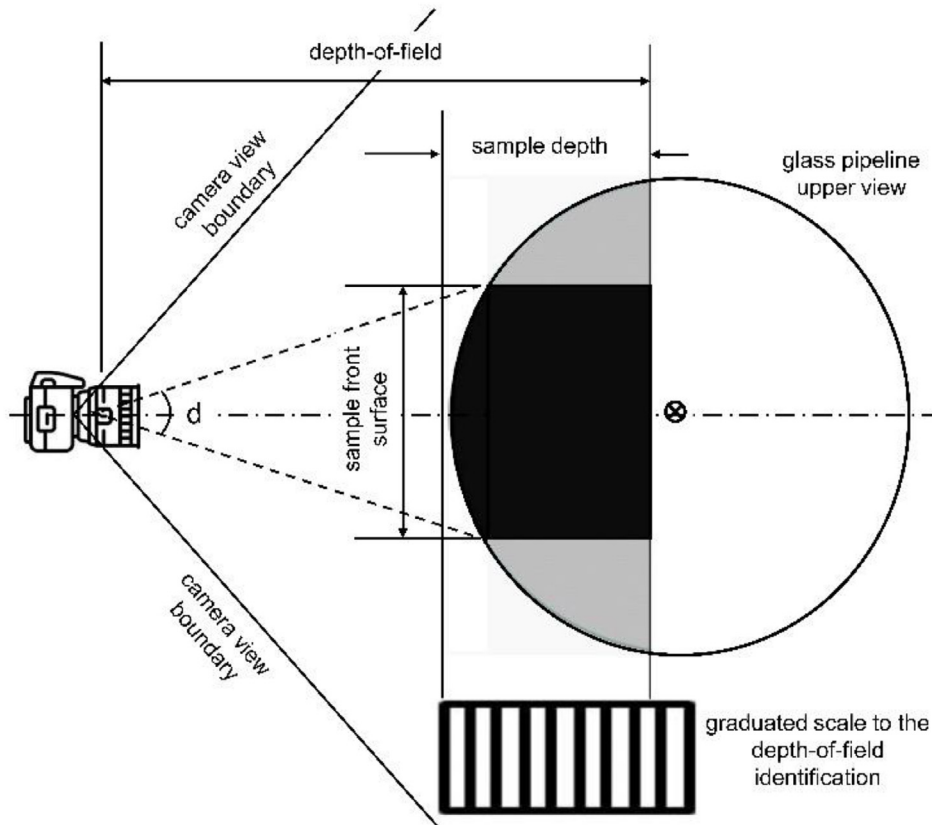


Fig. 16. Upper view of the experiment glass pipeline.

density (kg/m^3); ΔP_l is the pressure gradient due to the flow mixture drag; h is the measured water column difference in mm; L is the pressure taps' height difference in mm and g is the local gravity acceleration in m/s^2 . The gas-liquid density is obtained as a function of the average void fraction, $\langle \alpha \rangle$:

$$\rho_m = (1 - \alpha)\rho_L + \alpha\rho_G \quad (4.2)$$

where ρ_G is the gas density (kg/m^3).

Substituting (4.2) in (4.1) and adopting $\Delta\rho = \rho_G - \rho_L$, and neglecting the pressure difference due to the mixture friction considering

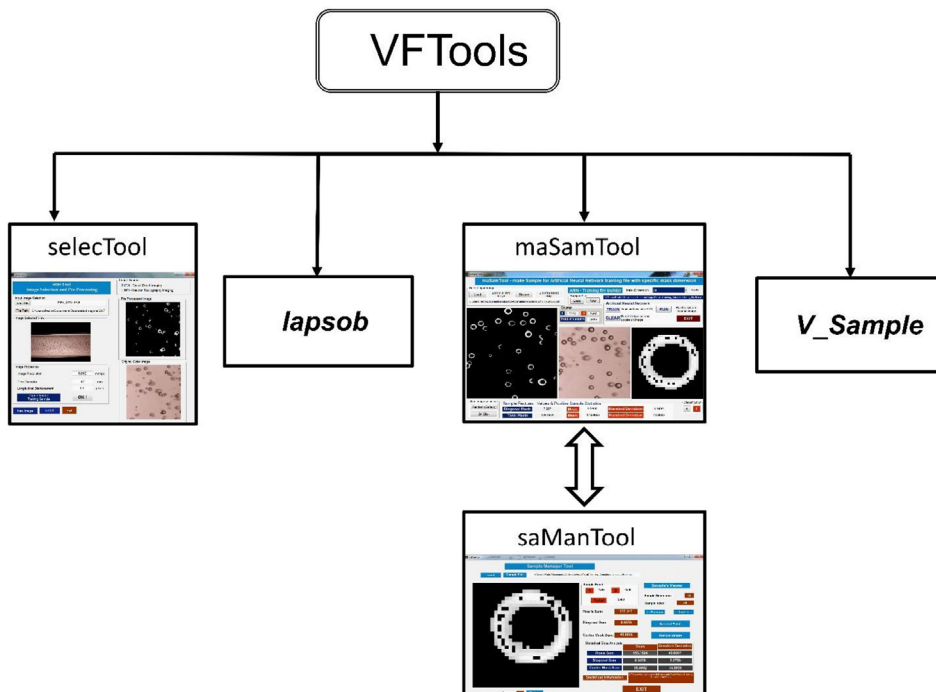


Fig. 17. VFTools modules.

the liquid phase velocity close to zero, the void fraction expression becomes:

$$\alpha = \frac{\rho_L}{\rho_L + \rho_G} \cdot \frac{h}{L} \quad (4.3)$$

Considering the calibration bench features, these constants where:

$$\begin{aligned} g &= 9,81 \text{ m/s}^2; \\ L &= 1295 \text{ m}; \\ \rho_L &= 997,82 \text{ kg/m}^3 (@ 15^\circ\text{C}, P_{\text{amb}}) \text{ and} \\ \rho_G &= 0,250 \text{ kg/m}^3 (@ 15^\circ\text{C}, P_{\text{amb}}) \end{aligned}$$

Detailed gravimetric method description is shown in Al-hadhrami et al. (2014) where an uncertainty analysis of this method is presented. This uncertainty is defined as the parameter related to the measure procedure that implicitly imbed dispersion when evaluating the superficial upper water film. The void fraction uncertainty, specifically for gravimetric method application, δ_α , could be computed by expression:

$$(\delta_\alpha)^2 = \left(\frac{\delta h}{L} \right)^2 + \left(\frac{h \cdot \delta L}{L^2} \right)^2 \quad (4.4)$$

5. VFTools modules

VFTools is composed by a set of modules used to compute the void fraction using two-phase flow images as the main input. These modules perform many tasks as the image sample selection, bubble recognition and geometric estimation, gas and liquid volumes, and final volumetric void fraction estimation. The set of modules and their interrelation is shown in Fig. 17.

The modules were developed using GUIDE (Graphic User Interface Development Environment) from MATLAB (Lent, 2013) to allow the system development and adjustments. Two modules, *lapsob* and *V_Sample* did not have GUIs.

5.1. Bubble border profile statistical analysis module

This module, called *lapsob*, makes statistical analyses based on two sets of selected border profiles from acquired bubble images classified as *in-focus* or *out-of-focus*. The module outputs final statistical parameters that will define the membership functions of the focal fuzzy inference system as presented in section 3.1, (Serra, 2017).

5.2. Two-phase flow volume sample computing module

Two-phase flow sample volume is computed by the *V_Sample* module with the input parameters and tube dimensions shown in Fig. 18. *V_Sample* inputs are the experiment geometrical parameters as the acquisition depth-of-field, " i_{dof} " and the sample depth-of-field, " s_{dof} ", the glass tube external diameter, " \varnothing_{ext} ", the glass thickness " $\Delta\varnothing$ ". The sample image is squared, so is assumed that the sample height "h" is the same that the front surface width, " S_p ".

Considering the sample front are to be a rectangle, the sample volume, " V_{gl} " is computed as the sample upper view area, " S_p " multiplied by its height, "h":

$$V_{gl} = S_p \cdot h \quad (5.1)$$

5.3. Image capture and preprocessing module

The input selection module is called *selecTool* and receives as input the image file as was stored by the acquisition experiment, and some acquisition parameters. Firstly, *selecTool* selects the front sample of 800×800 pixels' size. Afterward, the module estimates the focus segmentation threshold to be used in the fuzzy inference system based on the acquisition depth-of-field used.

5.4. RHTN modules

Two modules are responsible to integrate the Randomized Hough Transform with Artificial Neural Networks in the system: *maSamTool* which is main RHTN module and *saManTool* which gives support for

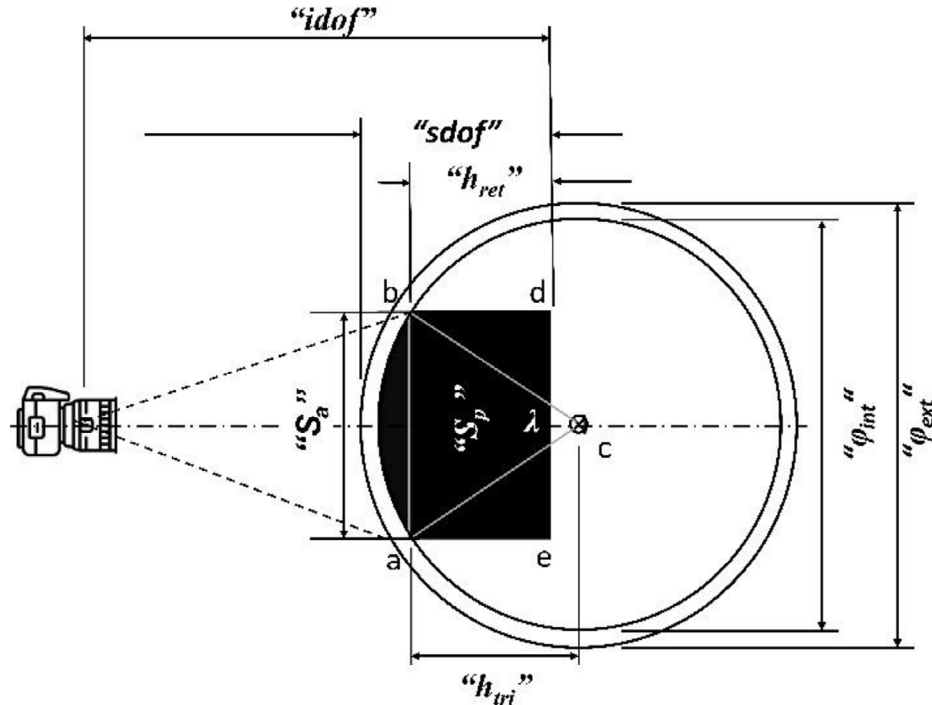


Fig. 18. Calibration bench upper view flow sample boundaries.

Table 2
Statistical estimates for fuzzy variables on *Experiment A*.

“in-focus” bubble borders			
Linguistic Variable	I_{if}	$(IS_{xy})_{if}$	$(IL_{xy})_{if}$
Mean	0.33615	0.51154	0.53455
Standard Deviation	0.09577	0.09311	0.16203
“out-of-focus” bubble borders			
Linguistic Variable	I_{oof}	$(IS_{xy})_{oof}$	$(IL_{xy})_{oof}$
Mean	0.47336	0.32559	0.47058
Standard Deviation	0.08838	0.09017	0.12065

Table 3
Statistical estimates for fuzzy variables on *Experiment B*.

“in-focus” bubble borders			
Linguistic Variable	I_{if}	$(IS_{xy})_{if}$	$(IL_{xy})_{if}$
Mean	0.44363	0.49546	0.65984
Standard Deviation	0.12544	0.11064	0.11195
“out-of-focus” bubble borders			
Linguistic Variable	I_{oof}	$(IS_{xy})_{oof}$	$(IL_{xy})_{oof}$
Mean	0.60171	0.32103	0.60348
Standard Deviation	0.09821	0.06800	0.12613

training samples' construction. The first module is used to construct the training samples, to perform the RHTN procedure, evaluating and erasing detected bubbles, and preparing new training samples with new sizes. This module also evaluates the volumes using accumulative variable. The second module, *saManTool* checks, ordinates and re-classifies bubble images from training samples. Finally, the *V_Sample* module evaluates the void fraction estimative.

6. Results and discussion

The FFIS setup required a prior bubble-profile statistical analysis. This analysis was performed based on two experiments:

➢ *Experiment A*: 128 two-phase flow selected images with 50 pixels/mm of resolution; 15 ± 3 mm of depth-of-field; glass tube external diameter of 42 mm and 4 mm of glass thickness; 800×800 pixels of front surface sample dimensions;

➢ *Experiment B*: 24 two-phase flow selected images with 53 pixels/mm of resolution; 20 ± 5 mm of depth-of-field; glass tube external diameter of 46 mm and 4 mm of glass thickness; 800×800 pixels of front surface sample dimensions.

6.1. Bubble border profile statistical analysis

The border-profiles' statistical estimates were used to establish the parameters in FFIS to define the “in-focus” and “out-of-focus” membership functions (Serra, 2017). Table 2 presents the statistical estimates on Experiment A, and Table 3 these estimates for Experiment B.

In Experiment A, the number of image samples used was 48 for *out-of-focus* and 48 for *in-focus* class. From each sampled bubble image, four image profiles were extracted resulting in 192 profiles for each class. Table 3 presents Experiment B estimates which used 24 samples resulting in 96 profiles for each class.

6.2. RHTN detections

The RHTN detection method resulted in a false-positive detection rate of 0.005% in the worst case. In this case, there were around 592000 ANN runs with 28 false-positive detections for a mask of 30×30 pixels.

An evaluation study was done for eleven ANN architectures varying the number of neurons to obtain less false-positive bubble detections. The initial choice to the number of neurons used in the ANN hidden layers was done based on the size of the mask used to track the image. The evaluated results pointed to an ANN initial configuration with 900 neurons for input layer, 144 neurons for the first hidden layer, 25 neurons for the second hidden layer and two neurons for the output layer. For this ANN configuration there was a false-positive detection rate of 0.004% for the same 30×30 sized mask.

Fig. 19 shows all detected bubbles by an ANN using a mask of 30×30 pixels' size on a flow image sample. This detection method was also used to evaluate and find the optimal number of ANN hidden layers and neurons in each layer, to minimize false-positive detections.

This initial ANN configuration is improved by more one input layer for each additional mask size used to scan images. In this paper we used mask-sizes with 30×30 , 36×36 , 44×44 , 54×54 , and 66×66 pixels.

Randomized Hough Transform with Artificial Neural Network, therefore, is used at two different moments of the computational system. In first place, it recognizes, and erases detected bubbles in the flow image during the construction of training samples. In a second

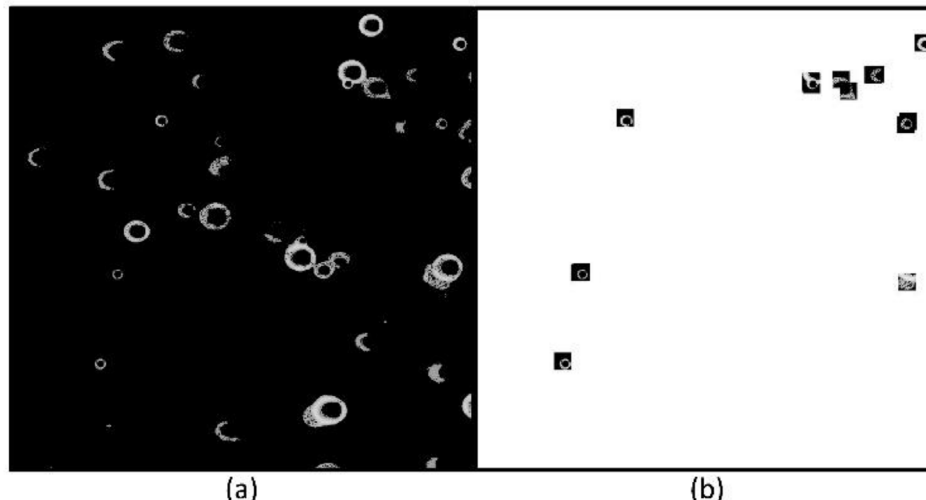


Fig. 19. Detected 30×30 pixels bubbles (b) from a flow image sample (a).

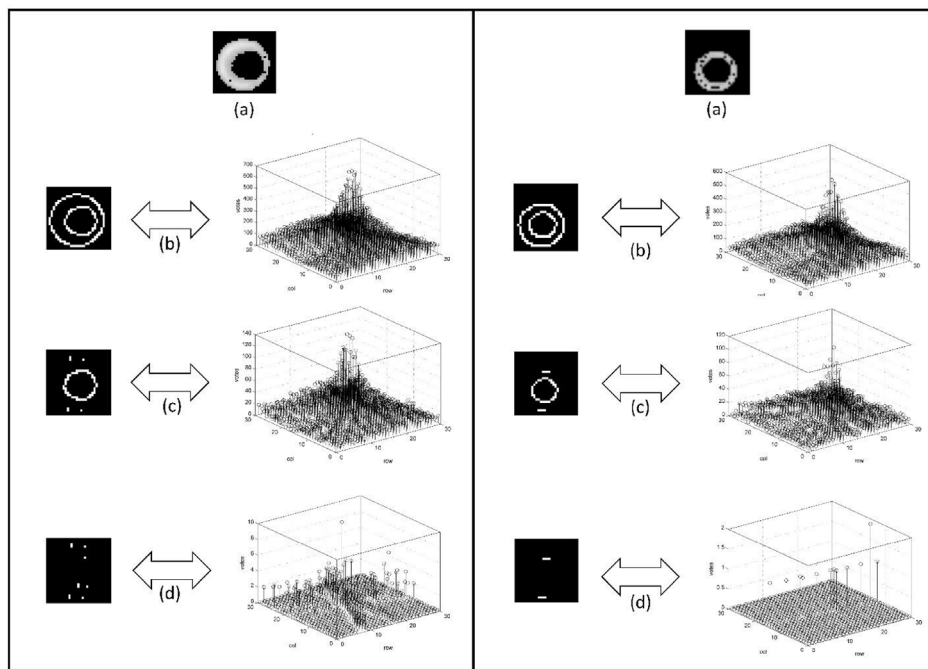


Fig. 20. RHTN steps for true-positive detections: (left column) well-focused bubble; (right column) bubble image with focus near FFIS threshold; (a) original images; (b) Canny operator detected borders and bubble-center voting histograms; (c) resulting images after erasing process and corresponding voting histograms; (d) images and histograms at last step.

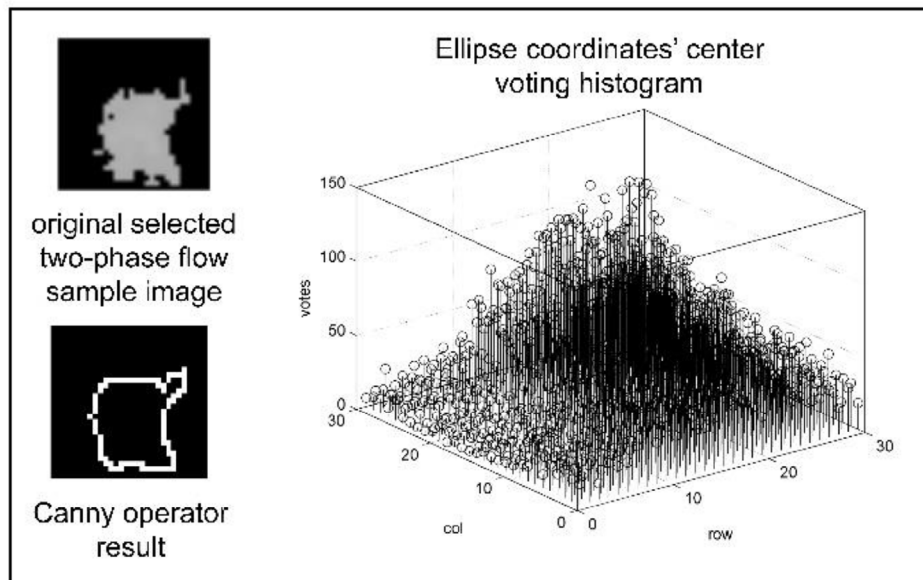


Fig. 21. RHTN false-positive process.

moment, RHTN is run to estimate the gas volume.

6.2.1. RHTN ‘one-bubble’ detection cases

6.2.1.1. True positive detections. RHTN ‘one-bubble’ detection steps are shown on Fig. 20 for two true-positive different cases. The figure presents, on the left side, a well-focused bubble case and, on the right side, a bubble detected with the focus near the FFIS threshold. Both columns of Fig. 20(a) represent original dimension-controlled images selected as “positive” by ANN.

Both columns of Fig. 20(b) refer to the border detection step where two borders are detected for each bubble. The external border is the *border-of-interest* as it represents the gas-liquid interface. Internal border represents the bubble boundary which is shadowed due to optical illumination effects. Randomized Hough Transform was performed over both borders to extract the geometrical parameters (center coordinates:

x_c, y_c ; minor and major semi axis: a, b and horizontal inclination angle: θ).

Fig. 20(c) and (d) illustrate the external border erasure steps where pixels identified as pertaining to this border are overwritten. This erasure process in steps is used to estimate the center of the ‘bubble’ using RHTN algorithm. Each new voting step finds a new geometrical center. The comparison of these different estimated centers is used as a criterium to determine if the evaluated internal ellipsoid shape is circumscribed to the previously evaluated external ellipsoid shape. If this condition is verified as true, then the parameters of the internal ellipsoid can be discarded, as it represents an internal bubble shadow. Otherwise it could represent an occluded bubble (as detailed in Section 3.3).

6.2.1.2. False-positive detections. False positive detections by ANN are

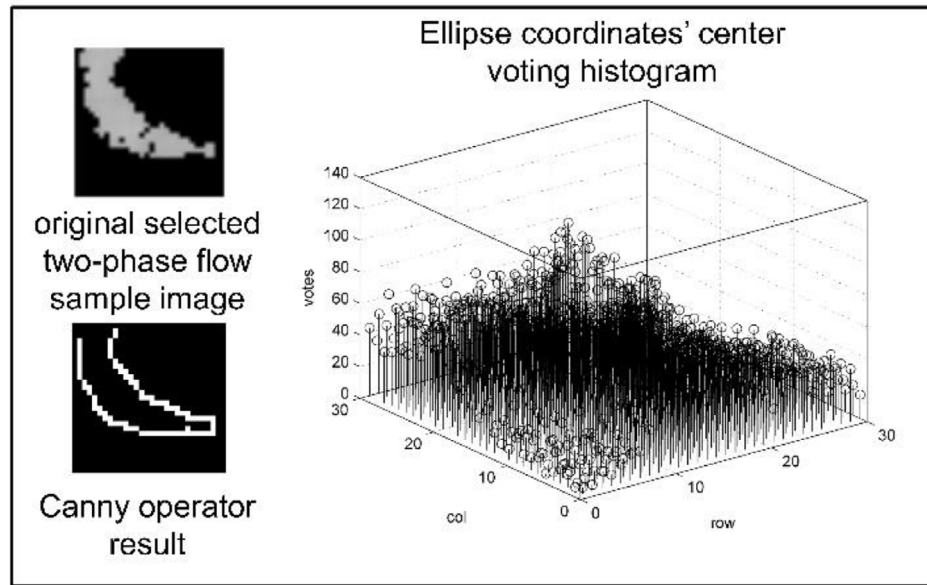


Fig. 22. RHTN false-positive process.

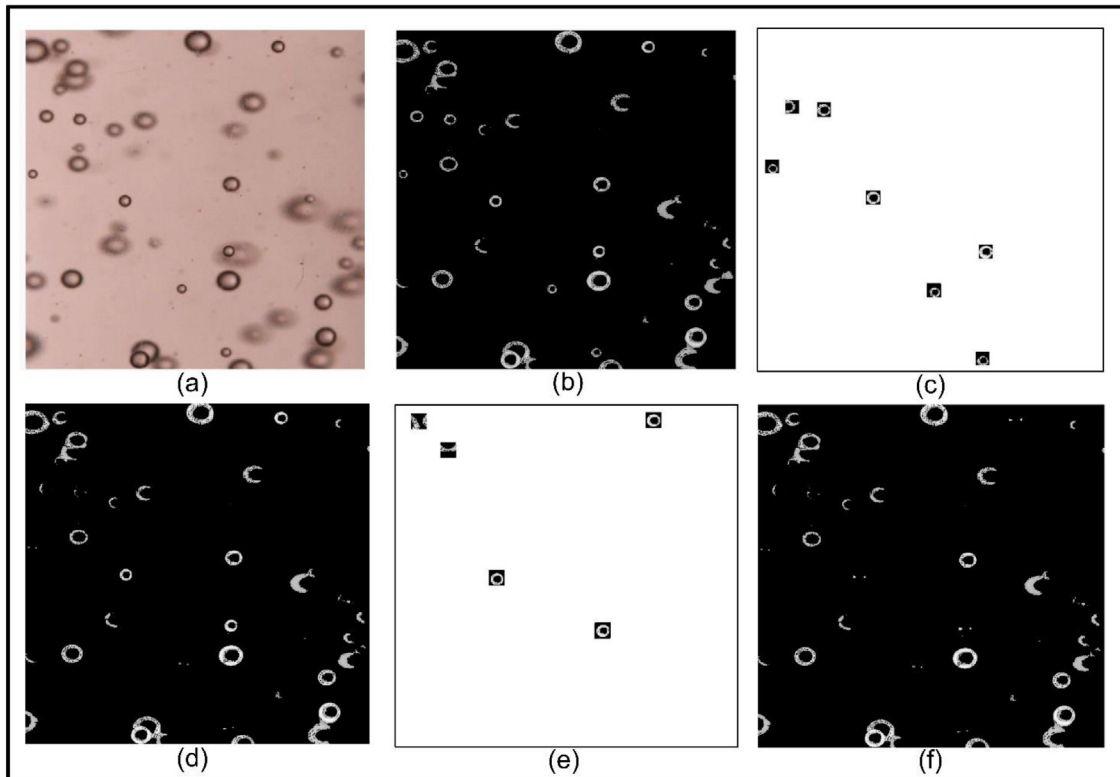


Fig. 23. RHTN detection sequence for 30×30 and 36×36 dimension-controlled mask selection: (a) original two-phase flow image sample; (b) segmented image based on FFIS estimation; (c) images of 30×30 pixels' size detected as bubble by ANN; (d) resulting image after the application of RHT and bubble erasing; (e) images of 36×36 pixels' size detected as bubble by ANN; (f) resulting image after the application of RHT and bubble erasing.

dealt by RHTN as “incomplete” or “out of expected shape” due to small pixel-detection rate when extracting geometrical parameters. Figs. 21 and 22 are instances of this occurrence. Fig. 21 shows a classical false-positive detection case. It's a typical ANN error and could be classified as inside the 0.005% range of false-positive detections as mentioned in 6.2 section. Canny operator detects a near squared border that is completely different from expected shapes (ellipse or circumference). Although this non-expected shape was detected, Randomize Hough

Transform considers these captured geometrical parameters as an ellipse. However, when the analytical shape is used to estimate RHT pixel detection rate, this detection is classified as false-positive. In this case, this rate was estimated to be 34.21% (lower than 55%).

A similar false-positive detection is shown in Fig. 22. Canny operator results suggest that the image is a partially *in-focus* bubble which could be an ellipse part, greater than the dimension-controlled mask size. Evaluated coordinate center is located outside of selected image. In

	Image #	Original image	Segmented image
Experiment B	1		
	2		
	3		
	4		
	5		
	6		
	7		
Experiment A	5		
	6		
	7		

Fig. 24. Segmented sampled images from experiments A and B.

this case, selection is discarded (or considered as false-positive) by RHTN the same way as the previous case (Fig. 21). Both RHTN results are identified as “no bubbles” detection and the selected image will not be erased from the two-phase flow sample image. This bubble could be counted as true positive when further detected by a larger dimension mask.

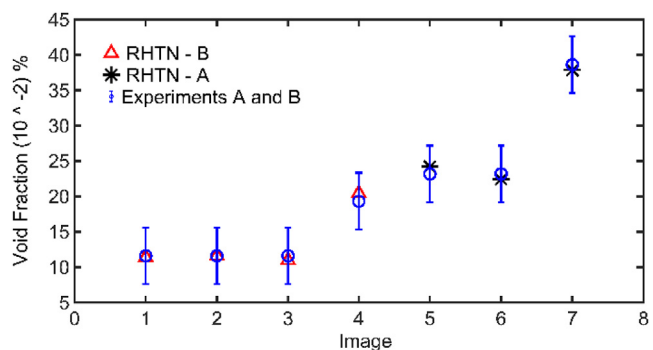


Fig. 25. RHTN estimation compared with experimental results.

6.2.2. Overall RHTN segmentation example

An overall RHTN segmentation example is shown in Fig. 23. This sequence shows the image scan cycle using a 30×30 pixels' mask followed by a 36×36 pixels' mask size. An original two-phase flow image sample is shown in Fig. 23(a). Fig. 23(b) shows the image after segmentation process based on FFIS. The following step is the bubble detection performed by ANN using 30×30 mask size, Fig. 23(c). Next step is the application of RHT transform over the segmented image and the corresponding pertinent erasing, Fig. 23(d). These two last steps are repeated until the two-phase flow sample image is completely tracked and the dimension-controlled mask size is increased to 36×36 pixels, also summarized in Fig. 23 (e) and (f). A set of images (original and segmented) samples used to estimate void fraction based on two experiments is shown on Fig. 24.

6.3. Void fraction estimation

Local void fraction estimation is done over the two-phase flow sample image by the evaluation of the ratio between the sample gas volume and the sample flow volume. It is important to emphasize that these experiments which are used to infer the void fraction were done at the calibration bench where there was only the presence of non-condensable gases (the air). This estimate is feasible if local void fraction can be approximated by the global void fraction over the circuit.

Experimental void fraction measured by gravimetric method, α_{exp} , is obtained through u-tube manometer reading of the water column difference, h . RHTN system estimates the corresponding sample void fraction, α_{co} . The ratio between estimations (γ) is computed using expression (6.1)

$$\gamma_i = \frac{\alpha_{co_i}}{\alpha_{exp_i}} \text{ where } i \text{ is the image number} \quad (6.1)$$

Images from two different experiments were used to adjust the RHTN estimation. Fig. 24 shows the two sets of images (800×800 pixels) used. These images were selected to estimate void fraction in the most difficult conditions. This difficulty arises from the summation of two main factors: the void fraction lowest possible values and the gravimetric intrinsic measurement method uncertainty.

These void fraction RHTN system values correspond to the larger dimension-controlled track mask used in these studies that pointed to an average adjustment factor, $\bar{\lambda}_A$, of 0.59, applied over experiment A images and, $\bar{\lambda}_B = 0.49$, applied to experiment B images. It's important to mention that a 1 mm of water level error (δh in Eq. (4.4)) in u-tube manometer corresponds to a void fraction uncertainty of 0.08% ($\delta\alpha$ in Eq. (4.4)) that is relevant in small void fraction cases. Fig. 25 shows this uncertainty by vertical error bars over the experimental estimation represented by small circles.

Void fraction RHTN – B estimation corresponds to experiment B images estimations by RHTN system and are represented by small ‘Δ’ points, similarly RHTN – A, to experiment A images estimations and are

represented by small “*” (Fig. 25). RHTN estimations showed in Fig. 25 consider the adjustment factor application over each RHTN system estimation by equations (6.2) and (6.3):

$$\bar{\lambda}_{exp} = \frac{\sum_{exp} \lambda_i}{n_{exp}} \quad (6.2)$$

$$\alpha_{RHTN-exp} = \left(\frac{1}{\bar{\lambda}_{exp}} \right) \cdot \alpha_{coexp} \quad (6.3)$$

where $\alpha_{RHTN-exp}$ are the adjusted void fraction values for A or B experiments (indicated by exp subscripts), n_{exp} is the images number of the experiment and α_{coexp} are the RHTN system estimation value for A or B image experiment. Fig. 25 shows the agreement of the RHTN system void fraction estimations compared with experimental values obtained for each image using u-tube manometer.

7. Conclusions and remarks

A new void fraction estimation methodology for two-phase flow cylindrical circuits was proposed. Although the experimental void fraction uncertainty is high (0.08%) in low void fraction measurements (0.05–0.4% values), RHTN estimation behavior showed good agreement with increasing void fraction values (Fig. 25).

This methodology is based on direct imaging and intelligent algorithms to infer gas volumes from detected bubbles. The method comprises image acquisition with controlled depth-of-field, fuzzy segmentation based on focus, and an algorithm fusing Hough transform and Artificial Neural Networks' sets to detect and evaluate bubble geometrical parameters. This RHTN algorithm showed to be a very efficient bubble detection technique with very low ‘false-positive’ cases (< 0.004%).

The fuzzy segmentation technique (FFIS), based on focus, enabled the system to estimate low vertical two-phase flow void fraction values based on 16 × 16 mm direct images. FFIS showed to be a promising tool to estimate the volume of the two phases present in acquired images. Future improvements on controlling acquisition image focus (depth-of-field) parameters and on segmentation techniques should improve this result.

RHTN has proven to be an efficient integration of ANNs with RHT in order to reduce ‘false-positive’ bubble detections. This method showed to be very efficient for partially occluded bubble detections due its voting threshold characteristics. RHTN has made use of a new voting process to ensure the geometrical center of ellipsoid shapes detection.

The void fraction estimation was done using adjustment factors. These factors are mainly dependent on bubble distribution homogeneity, geometrical and optical properties of cylindrical shaped tubes. This adjustment is necessary due proportion between local and total void fraction estimates. Studies based on larger void fraction values could validate this behavior.

Experiments and tests were initially applied for the most critical condition (very low void fraction values). Further studies to improve the method performance using a larger training database and greater void fraction values are being done and will be published elsewhere.

Acknowledgements

We acknowledge FINEP project ‘Desenvolvimento Científico e Tecnológico na Área Nuclear para Implantação do PNB’ under REDETEC-CNEN agreement number 01.10.0248.0, 2010, for part of image acquisition equipment.

Appendix A. Supplementary data

Supplementary data to this article can be found online at <https://doi.org/10.1016/j.pnucene.2019.103133>.

References

- Al-hadhami, L.M., Shaahid, S.M., Tunde, L.O., 2014. Experimental Study on the Flow Regimes and Pressure Gradients of Air-Oil-Water Three-phase Flow in Horizontal Pipes. Hindawi 2014.
- Barbosa, P.R., Selegihim Jr., P., Crivelaro, K.C.O., 2010. On the application of self-organizing neural networks in gas-liquid and gas-solid flow regime identification. J. Braz. Soc. Mech. Sci. Eng. XXXII, 15–20. <https://doi.org/10.1590/S1678-58782010000100003>.
- Bhardwaj, S., Mittal, A., 2012. A survey on various edge detector techniques. Procedia Technol. 4, 220–226. <https://doi.org/10.1016/j.protcy.2012.05.033>.
- Cleveland, J., Choi, J.H., 2009. Passive Safety Systems and Natural Circulation in Water Cooler Nuclear Power Plants. (Vienna, Austria).
- Coates, A., Carpenter, B., Case, C., Satheesh, S., Bipin, S., Wang, T., Wu, D.J., Ng, A.Y., 2011. Text detection and character recognition in scene images with unsupervised feature learning. In: International Conference on Document Analysis and Recognition. IEEE computer society, pp. 440–445. <https://doi.org/10.1109/ICDAR.2011.95>.
- Crivelaro, K.C.O., NETe, E. U. de S., Selegihim Jr., P., NETe, E.-U., de, S., Hervieu, E., DTP-D, C., à l'Energie, A., 2002. Detection of horizontal two-phase flow patterns through a neural network model. J. Brazilian Soc. Mech. Sci. 24. <https://doi.org/10.1590/S0100-73862002000100009>.
- Davies, E.R., 1987. A high speed algorithm for circular object location. Pattern Recognit. Lett. 6, 323–333. [https://doi.org/10.1016/0167-8655\(87\)90015-8](https://doi.org/10.1016/0167-8655(87)90015-8).
- De Mesquita, R.N., Masotti, P.H.F., Penha, R.M.L., Andrade, D.A., Sabundjian, G., Torres, W.M., MacEdo, L.A., 2012. Classification of natural circulation two-phase flow patterns using fuzzy inference on image analysis. Nucl. Eng. Des. 250, 592–599. <https://doi.org/10.1016/j.nucengdes.2012.06.014>.
- Elsalamony, H.A., 2016. Healthy and unhealthy red blood cell detection in human blood smears using neural networks. Micron 83, 32–41. <https://doi.org/10.1016/j.micron.2016.01.008>.
- Fichera, A., Muscato, G., Xibilia, M.G., Pagano, A., 2000. Modelling unstable behavior of a natural circulation loop with a neural network. Proc. Int. J. Conf. Neural Netw. 1, 75–80. <https://doi.org/10.1109/IJCNN.2000.857817>.
- Hsieh, C.C., Wang, S.B., Pan, C., 1997. Dynamic visualization of two-phase flow patterns in a natural circulation loop. Int. J. Multiph. Flow 23, 1147–1170.
- Krotov, E., 1987. Focusing. Int. J. Comput. Vis. 237, 223–237. <https://doi.org/10.1177/0020764011399004>.
- Kudariyawar, J.Y., Vaidya, A.M., Maheshwari, N.K., Satyamurthy, P., 2016. Computational study of instabilities in a rectangular natural circulation loop using 3D CFD simulation. Int. J. Therm. Sci. 101, 193–206. <https://doi.org/10.1016/j.ijthermalsci.2015.11.003>.
- Kumar, M., Pal, E., Nayak, A.K., Vijayan, P.K., 2015. Conceptual design of a passive moderator cooling system for a pressure tube type natural circulation boiling water cooled reactor. Nucl. Eng. Des. 291, 261–270. <https://doi.org/10.1016/j.nucengdes.2015.04.039>.
- Lent, C.S., 2013. Learning to Program with MATLAB: Building GUI Tools. John Wiley & Sons Inc.
- Mamdani, E.H., Assilian, S., 1999. An experiment in linguistic synthesis with a fuzzy logic controller.pdf. Int. J. Hum. Comput. Stud. 51, 135–147.
- Masotti, P.H.F., Mesquita, R.N., 2015. Paraconsistent logic study of image focus in cylindrical refraction experiments. In: Paraconsistent Intelligent-Based System, pp. 175–205.
- McLaughlin, R., 2000. Intelligent Algorithms for Finding Curves and Surfaces in Real World Data. (Western Australia).
- McLaughlin, R. a., 1998. Randomized hough transform: improved ellipse detection with comparison. Pattern Recognit. Lett. 19, 299–305. [https://doi.org/10.1016/S0167-8655\(98\)00010-5](https://doi.org/10.1016/S0167-8655(98)00010-5).
- Mendel, J.M., 1995. In: Fuzzy Logic Systems for Engineering: A Tutorial. IEEE. <https://doi.org/10.1016/0018-9219/95>.
- Nayak, A.K., Dubey, P., Chavan, D.N., Vijayan, P.K., 2007. Study on the stability behaviour of two-phase natural circulation systems using a four-equation drift flux model. Nucl. Eng. Des. 237, 386–398. <https://doi.org/10.1016/j.nucengdes.2006.05.009>.
- Nixon, M., 1990. Improving an extended version of the Hough transform. Signal Process. 19, 321–335. [https://doi.org/10.1016/0165-1684\(90\)90161-Q](https://doi.org/10.1016/0165-1684(90)90161-Q).
- Schmidhuber, J., 2015. Deep learning in neural networks: an overview. Neural Netw. 61, 85–117. <https://doi.org/10.1016/j.neunet.2014.09.003>.
- Serra, P., 2017. Cálculo da fração de vazão em escoamentos bifásicos (gás/líquido) a partir da identificação de bolhas em imagens digitais. Instituto de Pesquisa Energética e Nuclear/Universidade de São Paulo.
- Smith, T.R., Schlegel, J.P., Hibiki, T., Ishii, M., 2012. Two-phase flow structure in large diameter pipes. Int. J. Heat Fluid Flow 33, 156–167. <https://doi.org/10.1016/j.ijheatfluidflow.2011.10.008>.
- Sunde, C., Avdic, S., Pázsit, I., 2005. Classification of two-phase flow regimes via image analysis and a neuro-wavelet approach. Prog. Nucl. Energy 46, 348–358. <https://doi.org/10.1016/j.pnucene.2005.03.015>.
- Teng, Z., 2012. Ellipse detection: a simple and precise method based on randomized Hough transform. Opt. Eng. 51, 057203. <https://doi.org/10.1117/1.OE.51.5.057203>.
- Tsuji, S., Matsumoto, F., 1978. Detection of ellipses by a modified hough transformation. IEEE Trans. Comput. C 27, 777–781. <https://doi.org/10.1109/TC.1978.1675191>.
- Wang, H., Dong, F., 2009. Image features extraction of gas/liquid two-phase flow in horizontal pipeline by GLCM and GLGCM. 2009 9th. Int. Conf. Electron. Meas. Instr. 2–135, 2–139. <https://doi.org/10.1109/ICEMLI.2009.5274632>.
- Wang, M., Zhao, H., Zhang, Y., Su, G., Tian, W., Qiu, S., 2012a. Research on the designed

- emergency passive residual heat removal system during the station blackout scenario for CPR1000. Ann. Nucl. Energy 45, 86–93. <https://doi.org/10.1016/j.anucene.2012.03.004>.
- Wang, T., Wu, D.J., Ng, A.Y., 2012b. End-to-End text recognition with convolutional neural networks. In: Proc. 21st Int. Conf. Pattern Recognit. pp. 3304–3308.
- Woldesemayat, M.A., Ghajar, A.J., 2007. Comparison of void fraction correlations for different flow patterns in horizontal and upward inclined pipes. Int. J. Multiph. Flow 33, 347–370. <https://doi.org/10.1016/j.ijmultiphaseflow.2006.09.004>.
- Yip, R.K.K., Tam, P.K.S., Leung, D.N.K., 1992. Modification of hough transform for circles and ellipses detection using a 2-dimensional array. Pattern Recognit. 25, 1007–1022. [https://doi.org/10.1016/0031-3203\(92\)90064-\(P\)](https://doi.org/10.1016/0031-3203(92)90064-(P)).
- Yu, H., Liu, J., He, Z., 2008. A modified RHT method for ellipse detection based on geometric constraints and perceptual grouping. In: 3rd Int. Conf. Innov. Comput. Inf. Control. ICICIC'08 1–4, . <https://doi.org/10.1109/ICICIC.2008.45>.
- Zabulis, X., Papara, M., Chatziargyriou, A., Karapantsios, T.D., 2007. Detection of densely dispersed spherical bubbles in digital images based on a template matching technique. Application to wet foams. Colloids Surf. A Physicochem. Eng. Asp. 309, 96–106. <https://doi.org/10.1016/j.colsurfa.2007.01.007>.
- Zhang, J., Chen, R.H., Wang, M.J., Tian, W.X., Su, G.H., Qiu, S.Z., 2017. Prediction of LBB leakage for various conditions by genetic neural network and genetic algorithms. Nucl. Eng. Des. 325, 33–43. <https://doi.org/10.1016/j.nucengdes.2017.09.027>.
- Zhang, J., Shen, X., Fujihara, Y., Sano, T., Yamamoto, T., Nakajima, K., 2015. Experimental study on the safety of Kyoto University Research Reactor at natural circulation cooling mode. Ann. Nucl. Energy 76, 410–420. <https://doi.org/10.1016/j.anucene.2014.10.010>.
- Zhang, W.H., Jiang, X., Liu, Y.M., 2012. A method for recognizing overlapping elliptical bubbles in bubble image. Pattern Recognit. Lett. 33, 1543–1548. <https://doi.org/10.1016/j.patrec.2012.03.027>.